FINAL TECHNICAL REPORT

DYNAMICS OF SHEET CAVITATION
AND
LARGE SCALE SHEDDING

Charles L. Merkle, PhD
Principal Investigator

Grant Number: N00014-98-1-0311

May 30, 2000

20000612 097

REPORTDOCUMENTATIONPAGE

FormApproved
OMBNo.07040188

1.REPORTDATE *(DDMMYYYY)*	2.REPORTDATE	3.DATESCOVERED *(FromTo)*
30/05/00	5/30/00	2/1/98-7/31/99

4.TITLEANDSUBTITLE
Dynamics of Sheet Cavitation and Large Scale Shedding

5a.CONTRACTNUMBER

5b.GRANTNUMBER
N00014-98-1-0311

5c.PROGRAMELEMENTNUMBER

6.AUTHOR(S)
Dr . Charles L. Merkle

5d.PROJECTNUMBER

5e.TASKNUMBER

5f.WORKUNITNUMBER

7.PERFORMINGORGANIZATIONNAME(S)ANDADDRESS(ES)

The University of Tennessee Space Institute
411 B. H. Goethert Parkway
Tullahoma, TN 37388-9700

8.PERFORMINGORGANIZATION REPORTNUMBER

9.SPONSORING/MONITORINGAGENCYNAME(S)ANDADDRESS(ES)

Office of Naval Research, Atlanta Region
100 Alabama Street, SW, Suite 4R15
Atlanta, GA   30303-3104

10.SPONSOR/MONITOR'SACRONYM(S)

11.SPONSORING/MONITORING AGENCYREPORTNUMBER

12.DISTRIBUTIONAVAILABILITYSTATEMENT

Unlimited

13.SUPPLEMENTARYNOTES

14.ABSTRACT

See Attached

15.SUBJECTTERMS

16.SECURITYCLASSIFICATIONOF:			17.LIMITATIONOF ABSTRACT	18.NUMBER OFPAGES	19a.NAMEOFRESPONSIBLEPERSON
a.REPORT	b.ABSTRACT	c.THISPAGE			Dr. Charles L. Merkle
Unclassified			None	40	19b.TELEPONENUMBER(*Includeareacode)*
					931/393/7426

StandardForm298(Rev.898)
PrescribedbyANSIStdZ3918

DYNAMICS OF SHEET CAVITATION AND LARGE SCALE SHEDDING

Charles L. Merkle
University of Tennessee Space Institute
411 B.H. Goethert Parkway
Tullahoma, TN 37388

Introduction

Cavitation deals with the vaporization of a liquid as it flow past or through a body of interest. As the flow velocity increases and the local pressure decreases, the liquid can change to vapor if the overall pressure is sufficiently close to the vapor pressure. If the pressure change in a flowing liquid brings the liquid below its vapor pressure, local regions of the fluid can change phase and become vapor. In general, the phenomenon of cavitation increases as the overall pressure in the system is reduced.

While cavitation remains a very fascinating physical phenomenon, it also is of much interest in engineering circles because of the rapid damage cavitation can do to even the toughest materials. In the presence of cavitation, rapid pitting and other surface and structural damage can occur very quickly. For this reason improved understanding is needed to circumvent its damaging nature.

Cavitation occurs in many different forms. In some cases, cavitation occurs as a bubble cloud moving through the flowfield. Such cavitation is referred to as cloud cavitation. In other cases, cavitation appears as a bubble attached to the surface. This phenomenon is known as sheet cavitation. A third type of cavitation is vortex cavitation in which cavitation bubbles appear in the low-pressure core of a propeller tip vortex. The present report focuses on the second of these types, attached or sheet cavitation.

The dynamics of attached sheet cavitation are highly complex. The flowfield is two phase with both liquid and vapor being present. In nearly every case, the flowfield contains significant unsteady effects and the flow is generally three-dimensional. The multi-phase nature and the unsteadiness both increase the difficulty of making diagnostic measurements. The presence of the vapor phase can make the fluid opaque so that optical diagnostics cannot be employed. In addition, the unsteadiness makes it difficult to document the local nature of the flow. Despite these difficulties, large numbers of experiments have been conducted, and there is a considerable volume of data available in the literature. Certainly, this existing data has given much light on cavitation processes, but detailed local understanding of the cavitation phenomena is still lacking. The present study looks at applying detailed CFD computations to cavitating flowfields as an aid for guiding and improving experiments and as a means of providing increased understanding of the experimental results obtained to date.

Experimental observations of attached cavitation have provided us with a considerable understanding of cavitation processes. Experimental observations of cavitation on a hydrofoil have consistently shown that the surface pressure lies below the vapor pressure. In addition, the location at which cavitation appears generally exhibits a pressure that is somewhat below the vapor pressure for the fluid temperature of interest. The cavity can appear in the nose-region of a hydrofoil, at the mid-chord position, or near the trailing edge. A particularly appropriate study for the present analysis is the two-part study of Franc and Michel (1996). Their data clearly shows that the location at which cavitation appears on an isolated hydrofoil is a function of the angle of attack as well as the cavitation number.

Attached cavitation typically produces long, thin cavitation regions. The aft-end of the bubble is generally highly unsteady and is composed of a two-phase region in which the fluid in the vapor is converted back to liquid. The interface between the liquid and the vapor can be shiny or diffuse. A shiny interface generally implies that the interface is laminar, while a diffuse interface is generally characteristic of the presence of turbulence. Of particular interest is the experimental observation that the leading edge of the cavity can sometimes appear downstream of the minimum pressure point on a hydrofoil. This implies that the liquid successfully negotiates the lowest pressure region in the flowfield without changing to vapor, but then cavitates (or switches to vapor) at some higher pressure. This clearly suggests that non-equilibrium phenomena can be a part of the cavitation process.

Cavitation Models

Over the years a number of cavitation models have been used to study the cavitation process. The simplest of these treats the cavity as a constant pressure region that is filled with vapor. The pressure in the constant pressure cavity region is set equal to the vapor pressure of the liquid. The interface between the vapor and the liquid is then treated as a constant pressure streamline. The shape of the interface is dictated by the dynamics of the liquid flow and the trajectory of the constant pressure interface. Since the interface is a streamline, it is clear that in this 'cavitation' model, no cavitation occurs. The liquid flows around the bubble and the pressure of the liquid dictates the shape of the interface. The cavity consists of a fixed volume of vapor, but the vapor inside this bubble is quiescent. Consequently, this cavitation model does not involve cavitation at all (expect perhaps at very early times when the liquid inside the cavitation bubble was initially converted to vapor).

A major difficulty with this type of model is that it requires some 'closure' condition at the aft end of the cavitation bubble. The closure condition can take on several different forms, but one classical method is to use an artificial body or wall to guide the liquid back from the interface (which will normally be above the hydrofoil surface) so that it becomes attached to the hydrofoil surface once more. Combination of this simple cavitation model with a velocity potential model or a full Navier-Stokes formulation is

generally quite effective. The constant pressure cavitation region gives reasonable agreement with experiment, but it does lack fundamental understanding.

The emphasis in the present research is upon using a more physically realistic description of cavitation that can help to provide more mechanistic understanding of cavitation phenomena and can lead to improved understanding and control.

Present Approach

The modeling approach used in the present research is based upon highly resolved numerical solutions of the full Navier-Stokes equations coupled with a detailed model for the presence of cavitation. To provide an appropriate vehicle for incorporating the cavitation model, the Navier-Stokes equations are expressed in a generalized form that describes an arbitrary fluid with an arbitrary equation of state. The arbitrary fluid description facilitates the extension to a multi-phase model of cavitation.

To provide appropriate background, we start by writing the Navier-Stokes equations for a pure (single-phase, single-component) fluid. We then introduce the auxiliary cavitation model. Although most of our results are based upon a two-fluid model, we briefly summarize a single-fluid model that we have also tested. Both the single-fluid model and the two-fluid model follow directly from the generalized Navier-Stokes formulation.

The Navier-Stokes Equations: In vector notation, the equations of motion can be written as:

$$\Gamma \frac{\partial Q_p}{\partial \tau} + \frac{\partial Q}{\partial t} + \frac{\partial E}{\partial x} + \frac{\partial F}{\partial y} + \frac{\partial G}{\partial z} = v.t.$$

In this expression, (x, y, z) represents the Cartesian coordinates, t is the physical time describing unsteady transients, and τ represents a pseudo-time that is used for iteration at a given time step. The quantities $Q_p, Q, E, F,$ and G are vectors containing the primitive variables, the conservative variables, and the conserved fluxes in the x, y, and z directions respectively. They are given as,

$$Q_p = \begin{pmatrix} p \\ u \\ v \\ w \\ T \end{pmatrix} \quad Q = \begin{pmatrix} \rho \\ \rho u \\ \rho v \\ \rho w \\ \rho h^0 - p \end{pmatrix} \quad E = \begin{pmatrix} \rho u \\ \rho u^2 + p \\ \rho uv \\ \rho uw \\ \rho u h^0 \end{pmatrix} \quad F = \begin{pmatrix} \rho v \\ \rho uv \\ \rho v^2 + p \\ \rho vw \\ \rho v h^0 \end{pmatrix} \quad G = \begin{pmatrix} \rho w \\ \rho uw \\ \rho vw \\ \rho w^2 + p \\ \rho w h^0 \end{pmatrix}$$

The quantity, Γ, that multiplies the pseudo-time derivative is a matrix that is used to ensure that all terms in the equations are properly ordered so that the pseudo-time iteration converges efficiently under various limiting conditions.

The quantity, $v.t.$, signifies the diffusion or 'viscous' terms which are given by,

$$v.t. = \frac{\partial}{\partial x}\left(R_{xx}\frac{\partial Q_p}{\partial x}\right) + \frac{\partial}{\partial x}\left(R_{xy}\frac{\partial Q_p}{\partial y}\right) + \frac{\partial}{\partial x}\left(R_{xz}\frac{\partial Q_p}{\partial z}\right) + \frac{\partial}{\partial y}\left(R_{yx}\frac{\partial Q_p}{\partial x}\right) +$$

$$\frac{\partial}{\partial y}\left(R_{yy}\frac{\partial Q_p}{\partial y}\right) + \frac{\partial}{\partial y}\left(R_{yz}\frac{\partial Q_p}{\partial z}\right) + \frac{\partial}{\partial z}\left(R_{zx}\frac{\partial Q_p}{\partial x}\right) + \frac{\partial}{\partial z}\left(R_{zy}\frac{\partial Q_p}{\partial y}\right) + \frac{\partial}{\partial z}\left(R_{zz}\frac{\partial Q_p}{\partial z}\right)$$

The vector of dependent variables, Q_p, that appears inside the diffusion terms is the same variable that is used as the primary dependent variable on the left-hand side of the equation. Note that the vector that appears inside the physical time derivative is Q rather than Q_p. The change from Q to Q_p simplifies the computation without compromising the global conservation advantages of the conservative flux terms.

The quantities, R_{xx}, R_{xy}, etc. that appear in the diffusion terms are matrices that contain the diffusion properties of the fluid in question. In most cases of interest for cavitation modeling, the primary diffusion properties are the viscosity, μ, and the thermal conductivity, k. The physical properties of the fluid are the primary terms in the subject matrices. In general, all nine of these matrices are highly sparse. For a general compressible fluid for which the Stokes approximation has been made, these matrices take the form:

$$R_{xx} = \begin{pmatrix} 0 & 0 & 0 & 0 & 0 \\ 0 & \frac{4}{3}\mu & 0 & 0 & 0 \\ 0 & 0 & \mu & 0 & 0 \\ 0 & 0 & 0 & \mu & 0 \\ 0 & \frac{4}{3}\mu u & \mu v & \mu w & k \end{pmatrix} \qquad R_{xy} = \begin{pmatrix} 0 & 0 & 0 & 0 & 0 \\ 0 & 0 & -\frac{2}{3}\mu & 0 & 0 \\ 0 & \mu & 0 & 0 & 0 \\ 0 & 0 & 0 & 0 & 0 \\ 0 & \mu v & -\frac{2}{3}\mu u & 0 & k \end{pmatrix}$$

$$R_{xz} = \begin{pmatrix} 0 & 0 & 0 & 0 & 0 \\ 0 & 0 & 0 & -\frac{2}{3}\mu & 0 \\ 0 & 0 & 0 & 0 & 0 \\ 0 & \mu & 0 & 0 & 0 \\ 0 & \mu w & \mu v & -\frac{2}{3}\mu u & k \end{pmatrix}$$

$$R_{yx} = \begin{pmatrix} 0 & 0 & 0 & 0 & 0 \\ 0 & 0 & \mu & 0 & 0 \\ 0 & -\frac{2}{3}\mu & 0 & 0 & 0 \\ 0 & 0 & 0 & 0 & 0 \\ 0 & -\frac{2}{3}\mu v & \mu u & 0 & k \end{pmatrix} \qquad R_{yy} = \begin{pmatrix} 0 & 0 & 0 & 0 & 0 \\ 0 & \mu & 0 & 0 & 0 \\ 0 & 0 & \frac{4}{3}\mu & 0 & 0 \\ 0 & 0 & 0 & \mu & 0 \\ 0 & \mu u & \frac{4}{3}\mu v & \mu & k \end{pmatrix}\mu$$

$$R_{yz} = \begin{pmatrix} 0 & 0 & 0 & 0 & 0 \\ 0 & 0 & 0 & 0 & 0 \\ 0 & 0 & 0 & -\frac{2}{3}\mu & 0 \\ 0 & \mu & \mu & 0 & 0 \\ 0 & 0 & \mu w & -\frac{2}{3}\mu v & k \end{pmatrix}$$

$$R_{zx} = \begin{pmatrix} 0 & 0 & 0 & 0 & 0 \\ 0 & 0 & 0 & \mu & 0 \\ 0 & 0 & 0 & 0 & 0 \\ 0 & -\frac{2}{3}\mu & 0 & 0 & 0 \\ 0 & -\frac{2}{3}\mu w & 0 & \mu u & k \end{pmatrix} \qquad R_{zy} = \begin{pmatrix} 0 & 0 & 0 & 0 & 0 \\ 0 & 0 & 0 & 0 & 0 \\ 0 & 0 & 0 & \mu & 0 \\ 0 & 0 & -\frac{2}{3}\mu & 0 & 0 \\ 0 & -\frac{2}{3}\mu w & \mu v & \mu v & k \end{pmatrix}$$

$$R_{zz} = \begin{pmatrix} 0 & 0 & 0 & 0 & 0 \\ 0 & \mu & 0 & 0 & 0 \\ 0 & 0 & \mu & 0 & 0 \\ 0 & 0 & 0 & \frac{4}{3}\mu & 0 \\ 0 & \mu u & \mu v & \frac{4}{3}\mu w & k \end{pmatrix}$$

Note that the first row of all nine of the matrices, R_{xx}, R_{xy}, etc. is entirely zero. This corresponds to the well-known fact that the continuity equation contains no diffusion terms. Similarly, the first row of all nine matrices is zero, indicating that the pressure does not appear explicitly in the diffusion terms. The remaining term in the second, third and fourth rows describe the viscous forces that appear in the three components of the momentum equations. Note that only the viscosity appears in the second through fourth rows. The energy equation is the only row that contains multiple entries in each matrix. These multiple entries contain the heat conduction term (the diagonal term multiplied by the thermal conductivity), and the velocity components multiplied by the viscous

5

coefficient. The product of velocity and viscosity represents the viscous dissipation of kinetic energy into heat energy. These terms, taken together, describe the so-called viscous dissipation terms.

The equations of motion are completed by an equation of state, a thermodynamic relation that defines the enthalpy in terms of two other thermodynamic variables, and mathematical functions describing the viscosity and thermal conductivity as a function of two thermodynamic variables. Since the temperature and pressure both appear in our primary dependent variable, Q_p, we choose to express all four of these parameters as functions of the pressure an temperature. Thus, the equation of state is taken as an arbitrary function that relates the density to the temperature and pressure,

$$\rho = \rho(p,T)$$

The enthalpy is likewise given in terms of the pressure and temperature as,

$$h = h(p,T)$$

The transport properties (viscosity and thermal conductivity) are likewise expressed as arbitrary functions of pressure and temperature. For the viscosity,

$$\mu = \mu(p,T)$$

and for the thermal conductivity,

$$k = k(p,T)$$

Finally the stagnation enthalpy connects the enthalpy and the kinetic energy,

$$h^0 = h + \frac{1}{2}\left(u^2 + v^2 + w^2\right)$$

The Navier-Stokes equations given above, along with these four auxiliary relations, and the definition of the stagnation enthalpy gives a fully defined system that describes fluid flow under very generalized conditions. If the continuity equation is replicated so that it applies to multiple species or phases, the equations can likewise describe the flow of multi-component and/or multi-species flows. One of our cavitation models uses a two-phase description. Similarly we could include multiple momentum equations and/or multiple energy equations to cover these complexities.

We have tested two different cavitation models based on this general formulation. One uses a single-phase representation, while the other uses a two-phase description. These two models are described briefly below. As noted above, the two-phase model represents

6

our preferred model, but its characteristics are more properly put in focus by comparing it with the single-phase fluid.

Single-Phase Cavitation Model: The single-phase cavitation model was the first model we used to simulate the liquid/vapor phase change process. In this model, the density of the fluid is treated as a continuous, single-valued function of the pressure. To account for cavitation, we replace the discontinuous change in density at the cavitation pressure by a rapid, but continuous variation. For convenience, we also simplify the equation of state so that the density is a function of pressure only, $\rho = \rho(p)$, instead of a function of both pressure and temperature, $\rho = \rho(p,T)$. This allows us to replace the energy equation by the statement that the temperature is constant. This approximation is not necessary, but simplifies the analysis slightly in that the energy equation is uncoupled from the momentum equations for this 'compressible' fluid and need not be solved.

The net result of this single-phase cavitation model is that as the pressure is decreased below the vapor pressure the density of the water decreases from a value corresponding to that of a liquid to one corresponding to that of a vapor. A transition in the opposite direction occurs when the pressure is increased above the cavitation pressure. With this model, the density of the fluid in the vicinity of a hydrofoil rapidly decreases from liquid-like conditions to vapor-like conditions in a continuous manner as the surface pressure approaches the cavitation pressure. Making the density-pressure curve continuous rather than discontinuous as it is in under equilibrium conditions simplifies the numerical procedure while retaining much of the physical characteristics of the cavitation process.

In the computations, the pressure increment across which the transition between "liquid" and "vapor" regimes was accomplished was treated as a parameter. The transition between the two densities was parameterized by choosing a pressure increment, Δp, as a fraction of the dynamic pressure. Excellent results were obtained when Δp was set to 30-40% of the dynamic pressure, but solutions could also be obtained when it was reduced to a few percent. Dropping the temperature from the equation of state also decouples the energy equation from the equations of motion as in incompressible formulations although it is emphasized that the present formulation contains a finite speed of sound (in the transition region), and allows large changes in the density. This single-phase model therefore represents a simple approximation to cavitation in a constant temperature fluid.

In representative computations with this model, the pressure increment across which the transition from the 'liquid' to the 'vapor' regime was accomplished was treated as a parameter. The transition between the two densities was parameterized by choosing a pressure increment, Δp, as a fraction of the dynamic pressure and connecting the 'liquid' density with the 'vapor' density by a cubic equation that was first-derivative continuous at either end. Excellent results were obtained when Δp was set to 30-40% of the dynamic pressure, but solutions could also be obtained when it was reduced to a few percent. Representative pressure-density curves for the single-phase model are given in Fig. 1 for

a series of values of Δp. These curves give an indication of the shapes of the 'equations of state' used for the single-phase computations.

As was noted above, dropping the temperature from the equation of state decouples the energy equation from the equations of motion as in incompressible formulations. Nevertheless it is emphasized that the present formulation is fully compressible. It allows large changes in the density and results in a finite speed of sound. For a fluid with the equation of state, $\rho = \rho(p)$, the speed of sound is given by the square root of the pressure-density derivative,

$$c = \sqrt{\frac{dp}{d\rho}}$$

For the present single-phase computations, the equation of state was divided into three sections, a vapor region, a transition region, and a liquid region. In the vapor and liquid regions the density was taken as a linear function of pressure to give a quantitatively realistic speed of sound. In the transition region, the density was expressed as a cubic function of the pressure. The three regions are given as,

$$\rho = c_l^2 p \qquad\qquad\qquad p \le p_v - \frac{\Delta p}{2}$$

$$\rho = \rho_v + (\rho_l - \rho_v)\left[\left(\frac{1}{c_v^2} + \frac{1}{c_l^2} - 2\right)\left(\frac{p - p_v}{\Delta p}\right)^3 - \left(\frac{2}{c_v^2} + \frac{1}{c_l^2} - 3\right)\left(\frac{p - p_v}{\Delta p}\right)^2 + \frac{1}{c_v^2}\left(\frac{p - p_v}{\Delta p}\right)\right]$$

$$p_v - \frac{\Delta p}{2} \le p \le p_v + \frac{\Delta p}{2}$$

$$\rho = c_v^2 p \qquad\qquad\qquad p \ge p_v + \frac{\Delta p}{2}$$

In these expressions, p_l and p_v represent the pressure transition points, ρ_l and ρ_v are the corresponding densities, and $\Delta p = p_l - p_v$ signifies the width of the transition region. The quantities, c_l and c_v are the speeds of sound in the liquid and vapor. These values are taken from the literature. The liquid speed of sound, c_l was taken as 1510 m/s, corresponding to conditions in water at 293K. The speed of sound in vapor, c_v, was chosen as 420 m/s corresponding to the speed of sound in a perfect gas with a molecular weight of 18, and a specific heat ratio of 1.286 at 293K and one atmosphere.

The proportionality constants in the vapor and liquid regions in the example above are chosen to give a constant speed of sound in the pure media that is representative of that of the physical fluid. For computational purposes, this choice is arbitrary. The common

alternative of infinite speeds of sound (incompressible fluid) in each phase is equally valid. In the vapor region, the speed of sound should vary with local conditions, but a constant is appropriate for constant temperature vapor.

The speed of sound in the transition region varies continuously from the value in the pure vapor region to the value in the pure liquid region, but it reaches a quite low minimum in the intervening region. In particular, since the derivative of the pressure-density function is continuous at the liquid and vapor 'boundaries', the speed of sound at either end of the transition region is equal to that in the appropriate pure fluid. In the transition region, the speed of sound starts at the value corresponding to that of the vapor, then decreases rapidly to a very low value until near the end of the transition region at which point it increases rapidly until it reaches the speed of sound in the liquid. This continuous variation of the speed of sound in a mixture with a very low sound speed over most of the mixture region is typical of vapor-liquid mixtures. In the present case, the magnitude of the sound speed depends upon the width (Δp of the transition region. When Δp is increased, the speed of sound in the transition region increases. When Δp becomes very small the speed of sound in the transition region becomes very small. In the limit as Δp goes to zero $(d\rho / dp \rightarrow \infty)$, the speed of sound drops to zero. Consequently, supersonic velocities are easily encountered in the vicinity of the transition region. Representative curves showing the variation of the speed of sound in the transition region are given on Fig. 2 for a series of Δp's.

Preliminary results based upon this model were obtained for an ellipse, a NACA 66(mod) at one and four degrees angle of attack, and for flow over a cylinder. Results for the ellipse are given on Fig. 3 which shows Mach number curves for flow over an ellipse at minus 2 degrees angle of attack. Because the angle of attack is negative, the high velocity flow region occurs on the under side of the ellipse. The speed of sound in the single-phase liquid state is 1520 *m/s* (corresponding to the sound speed in water), so the Mach number there is on the order of 10^{-3}. Near the hydrofoil, the flow passes through the density transition shown on Figs. 1 and 2 where the speed of sound decreases rapidly. Consequently, the Mach number in the density transition region increases from nearly zero to above Mach 5 and then back to the incompressible regime in a very thin zone. Inside the high Mach number zone, the fluid is pure vapor, while outside it is pure liquid. Thus, the Mach number contours graphically describe the shape and size of an attached cavitation bubble on the underside of the ellipse near the leading edge.

Comparisons between the predictions from the single-phase model and experimental data from Shen and Dimotakis [1] for a NACA 66 hydrofoil were also made, but are not shown herein. The comparison indicated that the single-phase model could replicate the main features of sheet cavitation for both leading-edge and mid-chord cavitation. In particular quantities such as surface pressure and cavity length were predicted reasonably well. A series of different values of Δp (the width of the density-pressure transition) were used to ascertain the effect on cavity length and thickness. For cases where Δp was 20 - 40% of the dynamic pressure, reasonably good convergence to a steady solution was obtained. When the values of Δp were decreased to approximately 1% of the dynamic

9

pressure, the cavity interface became much sharper; however, the numerical stability of the algorithm deteriorated significantly, even with TVD shock capturing. Simulations could be run, but the values of the time-step were too small to obtained converged solutions. In assessing the results, it appeared that the reason for obtaining steady solutions was numerical rather than physical in nature. At larger values of Δp the interface between the liquid and the vapor was spread out over a number of grid points and this appeared to stabilize an otherwise unsteady flowfield. This steadiness disappeared as the width of the transition region was decreased. Further, for cases in which the transition region was too wide (i.e., the value of Δp was increased), the relatively small decrease in pressure did not allow the density inside the cavity to drop below the vapor density.

In addition to producing steady cavities, a second, and more fundamental, difficulty with the single fluid model is that it strictly enforces an equilibrium assumption on the cavitation process. With the single-fluid model, it is impossible for the cavity to start downstream of the low pressure point on the airfoil (as is observed experimentally). The single-fluid model requires that cavitation start as soon as the pressure reaches the vapor pressure. so that in all cases, the leading edge of the cavitation bubble will be ahead of the minimum pressure point. This effect is countered by the dual-phase model described below.

Dual-Phase Model: The dual phase model treats the cavitation problem by considering two distinct phases, a liquid phase and a vapor phase. Each phase is treated by a separate continuity equation, but a single momentum equation is used for the mixture. The transition between phases is modeled by a rate process which appears in the separate continuity equations as a source and a sink of each phase. In the present model, the effects of surface tension are ignored and both liquid and vapor are allowed to co-exist over a range of pressures. The use of a rate process for converting liquid to vapor and *vice-versa* allows the cavitation inception point to occur downstream of the minimum pressure point in agreement with experiment thereby giving it a meta-stable-like character.

To incorporate the two phases into the computational formulation, the equations of motion are augmented by adding a second continuity equation and by incorporating source terms to account for mass conservation during phase change. For treating the two phases, we introduce the volume fraction of vapor, or the void fraction, α_v, which represents the volume fraction of vapor present at any point. The volume fraction of liquid is then given as one minus the volume fraction of vapor $(\alpha_l = 1 - \alpha_v)$ since the sum of the volume fraction of liquid and vapor must be unity. From the volume fractions, the density of the mixture is then given by

$$\rho = \alpha_v \rho_v + (1 - \alpha_v)\rho_l$$

where ρ_l represents the density of the liquid phase, and ρ_v corresponds to the density of the vapor phase. The model for the two-phase mixture uses a different equation of state for each phase. The equations of state are analogous to the single-phase equation of state given above:

$$\rho_l = \rho_l(p,T), \quad \text{(liquid phase), and}$$

$$\rho_v = \rho_v(p,T), \quad \text{(vapor phase).}$$

The equations of motion of the two-phase system can then be written in a vector form analogous to that used above for the single-phase model.

Before going further, we digress to compare the volume fraction with the mass fraction and the mole fraction that are traditionally used in mixtures of gases. First of all, note that the volume fraction has the units:

$$\alpha_v = \frac{volume\ of\ vapor}{volume\ of\ mixture} = \frac{m_v^3}{m_{mix}^3}$$

The density function described here for the vapor (or for the liquid) has standard units of density:

$$\rho_v = \frac{mass\ of\ vapor}{volume\ of\ \text{vapor}} = \frac{kg_v}{m_v^3}$$

That is to say, the density of vapor (liquid) is defined as the mass of vapor (liquid) divided by the area that the vapor (liquid) occupies. As a result, the density of the mixture, $\rho = \alpha_v \rho_v + (1-\alpha_v)\rho_l$ has the units:

$$\rho = \alpha_v\rho_v + (1-\alpha_v)\rho_l = \frac{m_v^3}{m_{mix}^3}\frac{kg_v}{m_v^3} + \frac{m_l^3}{m_{mix}^3}\frac{kg_l}{m_l^3} = \frac{kg_v}{m_{mix}^3} + \frac{kg_l}{m_{mix}^3} = \frac{kg_{mix}}{m_{mix}^3}$$

Clearly, these are the correct units.

When the mass fraction, Y_v is used, the partial density is defined in a different manner. The mass fraction has the units,

$$Y_v = \frac{mass\ of\ vapor}{mass\ of\ mixture} = \frac{kg_v}{kg_{mix}}$$

and when multiplied by the density of the mixture we have,

$$\rho = Y_v \rho + (1 - Y_v)\rho = \frac{kg_v}{kg_{mix}} \frac{kg_{mix}}{m_{mix}^3} + \frac{kg_l}{kg_{mix}} \frac{kg_{mix}}{m_{mix}^3} = \frac{kg_v}{m_{mix}^3} + \frac{kg_l}{m_{mix}^3} = \frac{kg_{mix}}{m_{mix}^3}$$

By comparing units, we can relate the mass fraction to the void fraction as,

$$\rho Y_v = \alpha_v \rho_v = \frac{kg_{mix}}{m_{mix}^3} \frac{kg_v}{kg_{mix}} = \frac{m_v^3}{m_{mix}^3} \frac{kg_v}{m_v^3} = \frac{kg_v}{m_{mix}^3}$$

From the above relation, we can express a 'partial' density,

$$\hat{\rho}_v = \rho Y_v = \frac{mass\ of\ vapor}{volume\ of\ mixture} = \frac{kg_v}{m_{mix}^3}$$

The partial density corresponds to the density the vapor (liquid) would have if it were oblivious to the existence of the liquid (vapor) and occupied the entire volume assigned to the fluid. The partial density is the density that is typically used in multi-species mixtures of gases. Note we use the superscript caret to distinguish this partial density from the vapor density that appears when we use volume fractions. Also note that the units are different. The density of the vapor, ρ_v, is the mass of vapor divided by the volume the vapor occupies. The partial density, $\hat{\rho}_v$, is the mass of vapor divided by the total volume the fluid occupies. In the volume fraction expression, the density, ρ_v, represents the standard density—the total mass of vapor divided by the volume it occupies. In the mass fraction representation, the partial density denotes the total mass of vapor divided by the entire volume occupied by the mixture. This density implies that the vapor does not 'see' the liquid and responds just as though it were the only specie (phase) present. The difference between these two densities is exactly the difference in using Dalton's law of mixtures (for the mass fraction case) instead of Amagat's law (for the volume fraction case). Both are equivalent and both give the same answer. For computational purposes, there may however be a preference for one over the other.

The third way to express the mixture properties is in terms of the mole fraction,

$$X_v = \frac{moles\ of\ vapor}{mole\ of\ mixture} = \frac{mol_v}{mol_{mix}}$$

The mixture density is then obtained as,

$$X_v = \frac{M_{mix} Y_v}{M_v} = \frac{kg_v}{kg_{mix}} \frac{mol_v}{kg_v} \frac{kg_{mix}}{mol_{mix}} = \frac{mol_v}{mol_{mix}}$$

12

where M_{mix} represents the mean molecular weight of the mixture and M_v is the molecular weight of the vapor. From this relation, we find,

$$\rho Y_v = \alpha_v \rho_v = \frac{\rho M_v X_v}{M_{mix}}$$

but

$$\frac{\rho M_v}{M_{mix}} = \frac{kg_{mix}}{m_{mix}^3} \frac{kg_v}{mol_v} \frac{mol_{mix}}{kg_{mix}} = \frac{kg_v}{m_{mix}^3} \frac{mol_{mix}}{mol_v} \approx \frac{kg_v}{m_v^3}$$

where we have related the molecular weight to the volume. Consequently, the mole fraction is analogous to the volume fraction.

For two-phase flows the mass fraction and the volume fraction are equivalent, but generally the volume fraction works better.

$$\rho = X_v \rho_v + (1 - X_v)\rho_l = \frac{m_v^3}{m_{mix}^3} \frac{kg_v}{m_v^3} + \frac{m_l^3}{m_{mix}^3} \frac{kg_l}{m_l^3} = \frac{kg_v}{m_{mix}^3} + \frac{kg_l}{m_{mix}^3} = \frac{kg_{mix}}{m_{mix}^3}$$

Formulation for Time-Accurate Computations: The above development applies to steady state flows only. For the cavitation problem, it is imperative that we consider time-accurate flows to be able to simulate the unsteadiness that is characteristic of flows with attached sheet cavitation. For implementation in a time-accurate sense, we write the dual-time version of the two-phase equations. We include the physical time as part of a four-dimensional divergence (x, y, z, t) operator and add a pseudo-time term, τ, for the iterations at each time step (or for iteration to the steady state if the physical time derivative term goes to zero). We then use conservation variables, $Q = \left(\rho, \rho u, \rho v, \rho w, \rho h^0 - p\right)^T$ in the physical time derivative and the primitive variables in the pseudo-time derivative along with a preconditioning matrix. The resulting vector form then becomes:

$$\Gamma \frac{\partial Q_p}{\partial \tau} + \frac{\partial Q}{\partial t} + \frac{\partial E}{\partial x} + \frac{\partial F}{\partial y} + \frac{\partial G}{\partial z} = H + v.t.$$

where H represents the source (and sink) terms in the continuity equations representing phase changes.

The two continuity equations can be expressed as one equation for the liquid and one for vapor phase or as the global continuity equation (the sum of these two) and either of the phasic equations. Here we express the system in terms of the total conservation of mass

13

equation (the sum of the liquid and gas phase equations) and the liquid phase conservation equation. With this choice, the terms in the equations become,

$$
Q_p = \begin{pmatrix} p \\ u \\ v \\ w \\ T \\ \alpha_l \end{pmatrix} \quad
Q = \begin{pmatrix} \rho \\ \rho u \\ \rho v \\ \rho w \\ \rho h^0 - p \\ \rho_l \alpha_l \end{pmatrix} \quad
E = \begin{pmatrix} \rho u \\ \rho u^2 + p \\ \rho uv \\ \rho uw \\ \rho u h^0 \\ \rho_l \alpha_l u \end{pmatrix} \quad
F = \begin{pmatrix} \rho v \\ \rho uv \\ \rho v^2 + p \\ \rho vw \\ \rho v h^0 \\ \rho_l \alpha_l v \end{pmatrix} \quad
G = \begin{pmatrix} \rho w \\ \rho uw \\ \rho vw \\ \rho w^2 + p \\ \rho w h^0 \\ \rho_l \alpha_l w \end{pmatrix}
$$

The system is completed by specifying two equations of state:

$$\rho_l = \rho_l(p,T), \quad \text{and} \quad \rho_v = \rho_v(p,T),$$

given earlier, along with the definition of the mixture density,

$$\rho = \alpha_l \rho_l + (1 - \alpha_l)\rho_v$$

The system is then closed by specifying analogous thermodynamic relations for the enthalpy of each phase,

$$h_l = h_l(p,T) \quad \text{and} \quad h_v = h_v(p,T)$$

The mixture enthalpy relation likewise follows the relation for the total density,

$$\rho h = \alpha_l \rho_l h_l + (1 - \alpha_l)\rho_v h_v$$

The important properties that appear in the Jacobian of the flux term and also in the preconditioning matrix are given by differentiating the density function(s) in the continuity equation(s) to get the partial derivatives of density with respect to pressure, temperature and volume fraction. These are most readily obtained by computing the Jacobian,

$$
\frac{\partial Q}{\partial Q_p} = \begin{pmatrix}
\rho_p & 0 & 0 & 0 & \rho_T & \rho_\alpha \\
\rho_p u & \rho & 0 & 0 & \rho_T u & \rho_\alpha u \\
\rho_p v & 0 & \rho & 0 & \rho_T v & \rho_\alpha v \\
\rho_p w & 0 & 0 & \rho & \rho_T w & \rho_\alpha w \\
-(1 - \rho h_p) & \rho u & \rho v & \rho w & \rho h_T & \rho h_\alpha \\
\rho_{lp} \alpha_l & 0 & 0 & 0 & \rho_{lT} \alpha_l & \rho_l
\end{pmatrix}
$$

14

where subscripts refer to partial differentiation. For example, the terms with the subscript, p, represent derivatives with respect to the pressure, and are defined as:

$$\rho_{lp} \equiv \left(\frac{\partial \rho_l}{\partial p}\right)_{u,T,\alpha} \qquad \rho_{vp} \equiv \left(\frac{\partial \rho_v}{\partial p}\right)_{u,T,\alpha}$$

and

$$\rho_p \equiv \left(\frac{\partial \rho}{\partial p}\right)_{u,T,\alpha} = \alpha_l\left(\frac{\partial \rho_l}{\partial p}\right)_{u,T,\alpha} + (1-\alpha_l)\left(\frac{\partial \rho_v}{\partial p}\right)_{u,T,\alpha} = \alpha_l\rho_{lp} + (1-\alpha_l)\rho_{vp}$$

The terms with the subscript, T, represent derivatives with respect to the temperature. They are defined as,

$$\rho_{lT} \equiv \left(\frac{\partial \rho_l}{\partial p}\right)_{p,u,\alpha} \qquad \rho_{vT} \equiv \left(\frac{\partial \rho_v}{\partial T}\right)_{p,u,\alpha}$$

and

$$\rho_T \equiv \left(\frac{\partial \rho}{\partial T}\right)_{p,u,\alpha} = \alpha_l\left(\frac{\partial \rho_l}{\partial T}\right)_{p,u,\alpha} + (1-\alpha_l)\left(\frac{\partial \rho_v}{\partial T}\right)_{p,u,\alpha} = \alpha_l\rho_{lT} + (1-\alpha_l)\rho_{vT}$$

Finally the derivative with respect to the volume fraction, α_l, also appears. This term is

$$\rho_\alpha \equiv \left(\frac{\partial \rho}{\partial \alpha_l}\right)_{p,u,T} = \rho_l - \rho_v$$

Note that derivatives of the individual densities with respect to the volume fraction are identically zero since the phasic densities do not depend upon the volume fraction,

$$\left(\frac{\partial \rho_l}{\partial \alpha_l}\right)_{p,u,T} = 0 \qquad \left(\frac{\partial \rho_v}{\partial \alpha_l}\right)_{p,u,T} = 0$$

The viscous terms in the two-phase equation system are identical to those given above except for the additional equation and are not re-written.

The primary new term in the equations for the two-phase system is the source term, H, which ensures local conservation of mass when liquid changes to vapor or when vapor

15

changes to liquid. These source terms correspond to the phase transition model. For the liquid volume fraction equation, the source term includes one contribution that describes the rate of conversion of vapor to liquid and one for the conversion of liquid to vapor. The conversion from vapor to liquid appears as a source term in the liquid volume fraction equation, while the conversion from liquid to vapor appears as a source term. These terms appear on the right hand side of the conservation equation and take the form,

$$\rho_{lp}\frac{\partial \alpha_l}{\partial \tau} + \frac{\partial \rho_l \alpha_l}{\partial t} + \frac{\partial \rho_l \alpha_l u}{\partial x} = -\frac{\alpha_l}{\tau_l} + \frac{(1-\alpha_l)}{\tau_v}$$

where τ_l and τ_v are the characteristic times for conversion from liquid to vapor and from vapor to liquid respectively. These times are chosen as being proportional to the local pressure difference,

for $p \le p_v$: $\quad \frac{1}{\tau_l} = 0;$ $\qquad \frac{1}{\tau_v} = \frac{l}{\tau_r}\left|\frac{p-p_v}{q}\right|$ $\quad$ and

for $p \ge p_v$: $\quad \frac{1}{\tau_l} = \frac{1}{\tau_r}\left|\frac{p-p_v}{q}\right|;$ $\qquad \frac{1}{\tau_v} = 0$

A representative choice with $K = (K_v / K_l) = 1/(\alpha_l + \rho_v / \rho_l)$ is shown on Fig. 2 for various values of K ranging from 1.0 to .001. The corresponding ratio of the speed of sound in the two-phase mixture to the speed of sound in the liquid is given on Fig. 3. This figure shows the familiar minimum in the sound speed when changing from 100% vapor to 100% liquid. Note that in the case where the liquid and vapor densities are equal, that no minimum speed of sound appears between the liquid and gas phases.

Franc-Michel Experiment: Franc and Michel [1,2]have reported a series of cavitation experiments on hydrofoils that are appropriate for calibration and validation purposes in the above models. Their experiments show that turbulent spots from exploding nuclei can remove sheet cavitation, but that leading edge sheet cavitation is resistant to the presence of free-stream nuclei and to the boundary layer state, whether it is laminar or turbulent. Their cavitation results show that the cavitation pattern is two dimensional near the leading edge where it appears at large angles of attack and high cavitation numbers. Mid-chord cavitation appears at middle angles of attack and middle values of the cavitation number. Mid-chord cavitation tends to be three dimensional. When the angle of attack and the cavitation number are both low, cavitation occurs at the trailing edge. Trailing edge cavitation is generally predominantly two dimensional.

Careful sequences of measurements show that cavitation moves from the trailing edge to the leading edge as the angle of attack is increased. In general, attached cavitation is established downstream of boundary layer separation, but as the number of free-stream nuclei increases, cavitation moves toward the minimum pressure point. When the

boundary layer transitions from the laminar to the turbulent state, the turbulence generally eliminates attached cavitation. Finally, Franc and Michel's experiments show that for selected angles of attack, decreasing the cavitation number can cause cavitation to first appear, then disappear and finally reappear again. This non-monotonic behavior and particularly the fact that decreasing the cavitation number causes cavitation to disappear suggests that non-equilibrium effects are present.

Predictions from Two-Phase Model: A series of computations has been computed with the dual-phase model. In general, these results are unsteady and exhibit fluctuations around the trailing edge, and in some cases the leading edge, of the cavitation region. As the cavitation number decreases (and the size of the cavitation bubble increases), the flowfield becomes more and more unsteady. Some representative results from the two-phase cavitation model are discussed in the present section. Most of the results shown have been computed on a multi-block grid involving typically 20 to 30 blocks, although where noted the results have been obtained on a single-block grid. Representative grids are shown on Figs. 6 and 7 for both the near field and the far field. The plots that show the multi-block results include the outline of the multiple blocks. The present two figures are for grids of 30,000 nodes each. The multi-block configuration in Fig. 6 uses 30 blocks.

As a first example of the predictions from the two-phase model, we show results for flow over the NACA 66 (mod) hydrofoil used in the Shen-Demotakis experiment referred to above. Figure 8 shows the density and pressure contours for flow at 4 degrees angle of attack and a cavitation number of 0.91. The Reynolds number is one million, and the density ratio between liquid and vapor was taken as 100. Since the density is constant over the entire liquid region, the density contours appear only in the cavitation bubble region. The pressure contours, however, are distributed over the entire flowfield and, in a qualitative sense, retain the familiar pressure distribution of single-phase flows. Close inspection of the flow near the cavitation region, however, shows the pressure is essentially constant inside the cavity as is frequently assumed in simple cavitation models. We note that the pressure in this region does retain weak variations rather than being strictly constant. In addition, the (nearly) constant pressure region appears as a result of the computation, not as the result of an assumption in the modeling. Again, the background segments in the plot represent boundaries of the multi-blocks, and are not a part of the solution.

A close-up view of the details in the cavitation region for this same computation is shown in Fig. 9. The velocity vectors in this region show the presence of a re-entrant jet on the downstream end of the cavitation region. This narrow re-entrant jet flows forward against the free-stream flow direction and lies between the rear-most part of the cavity and the surface of the hydrofoil. In addition, the flowfield gives the suggestion that a portion of the cavity is about to be shed into the wake. Long-term computations do show that the cavity length fluctuates slowly as the result of such periodic shedding.

17

Figure 10 shows the pressure contours over a wedge patterned after experiments by Ceccio. This figure shows the pressure contours on the fully wetted wedge as a function of the distance along the wedge surface. The results contrast the pressure contours when cavitation is present with those when the wedge surface is fully wetted. The presence of cavitation shows a decided change in the surface pressure that should be measurable experimentally.

The next several figures concern the flow over a NACA 16-012 hydrofoil like that used in the Franc and Michel experiments. Both multi-block and single-block grid computations were obtained for this airfoil. In both cases, the grid contained from 20,000 to 50,000 grid points. The intent of these computations was to provide a fine enough grid structure to ensure that the conclusions deduced from the results were not grid dependent. The following figures show representative solutions on these and similar grids.

Fig. 11 shows an attempt at a laminar flow solution over the NACA 16-012 hydrofoil. The flow conditions of interest were, of course, turbulent, but a series of laminar flow solutions were attempted to understand the underlying flowfield without the uncertainties introduced by a turbulence model. For all but the very lowest Reynolds number conditions attempted, the laminar solutions resulted in laminar separation at the trailing edge, and the resulting flowfield was highly unsteady. Figure 11 shows the flowfield at one instant of time in a computation at a Reynolds number of 75,000. The highly unsteady flowfield is clearly indicated here.

The emphasis in modeling cavitation is on finding hydrofoils that contain laminar flow over the leading edge where the cavity develops, but turbulent flow over the trailing edge to prevent laminar separation and to stabilize the flowfield. The present laminar computations demonstrated amply that the unsteadiness from a completely laminar solution would not allow cavitation studies to be done without a turbulence model. It is imperative in cavitation studies, however, that the turbulence model provide a non-cavitating flowfield that is qualitatively proper. Specifically this means that the flow must be laminar over the leading edge of the hydrofoil to allow cavitation, but turbulent at the trailing edge to prevent separation. Experimental evidence shows that the presence of turbulent flow near the leading edge prevents the formation of attached sheet cavitation. The present model is probably not sensitive to the presence of turbulence in establishing cavitating regions, but it is important to establish a correct flowfield to enable later improvements.

One of the characteristics of the Franc-Michel experiments is the manner in which the cavitation position moves from the trailing edge to the leading edge. Franc and Michel also noted that the locations of transition to turbulence and separation likewise varied with angle of attack. The present results are computed with the k-e model, and the free-stream turbulence has been carefully adjusted to get the transition location and the turbulence behavior to match that of the experiments. Results for two different levels of free-stream turbulence are illustrated below to indicate the manner in which the flowfield changes with the turbulence level, and the sensitivities involved in matching the fully wetted airfoil experiments.

18

As a first example of the effects of a turbulence model, we present on Fig. 12 the velocity contours and the ratio of the eddy viscosity to the laminar viscosity for the NACA 16-012 hydrofoil at zero degrees angle of attack. The present computation uses third-order upwind differencing and implicit discretization in time and is for a cavitation number at which the flow is fully wetted and cavitation does not occur. As can be seen from the figure, the solution, both in terms of the velocity and the turbulence level is symmetric about the hydrofoil as would be expected. The level of free-stream turbulence in this zero-degree condition has been adjusted to match the experimental observations at this flow condition. Hereafter, we refer to this free stream turbulence level as the 'low' turbulence level. As seen in the figure, the effects of turbulence are significant only in the boundary layers near the trailing edge (approximately the last 10%) of the hydrofoil and in the wake behind the hydrofoil. This local turbulent region is, however, sufficient to remove the large-scale unsteadiness that was observed in the laminar calculation at Re = 75,000 (Fig. 10). In contrast to that laminar case, the present turbulent case converged very well to a steady state solution with a very small recirculation zone at the trailing edge. Again, both the steady solution and the presence of turbulence over the aft 10% of the hydrofoil are in agreement with the Franc and Michel measurements.

Corresponding results for the NACA 16-012 hydrofoil at three degrees angle of attack are shown on Figs. 13 and 14. The chord Reynolds number for this case is again 300,000 and the same grid and solution procedures were used. Figure 13 shows contours of the velocity and the ratio of turbulent to laminar viscosity for this three-degree angle of attack. Here the velocity clearly shows non-symmetric (upper-to-lower surface) contours because of the angle of attack. The eddy viscosity likewise shows a similar asymmetry. The interesting fact is that turbulence starts at about mid-chord on the upper surface, while its transition region on the lower surface is closer to the trailing edge than in the zero-degree angle of attack case.

The corresponding pressure contours for the three-degree angle of attack case are given on Fig. 13 along with a plot of the multi-block grid that was used for the computations. The computed pressure distribution on the surface is in good agreement with experimental measurements at these conditions. Again, the flowfield at $\alpha = 3$ degrees results in a well converged, steady solution. Finally, a near-field view of the ratio of turbulent to laminar viscosity is shown on Fig.15. More details of the asymmetry in this figure are discussed below.

The effect of the freestream turbulence level on the flowfield solution is shown on Figs. 16 and 17 for two different free-stream turbulence levels. Figure 16 shows the solution for the 'low' freestream turbulence conditions of the results in Figs. 12 to 15. The top half of Fig. 16 shows a near-field view of the velocity vectors over the rear portion of the airfoil for the zero-degree angle of attack, while the bottom half shows the results for the three-degree case. Similar results are shown on Fig. 17 for a high free stream turbulence level.

Changing the free-stream turbulence level for the zero-degree angle of attack case (the top plots of Figs. 16 and 17) has very little effect on the results. The velocity vectors in both cases are quite similar. (Note that the A different (single block) grid was used for the high turbulence results on Fig. 17 (this grid is given in Fig. 7), so that the locations of the velocity vectors is somewhat different, but overall the two results are qualitatively similar.

Results for the three-degree angle of attack are, however, considerably different. The high free-stream turbulence calculation (Fig. 17) shows a thick turbulent boundary layer on the upper side of the airfoil and a thin one on the lower side, while the low free-stream turbulence case (discussed above) shows a thicker boundary layer on the lower surface. Close inspection of this result shows that the reason that the boundary layer is thicker on the lower surface is that there is a separation region at about 85% chord. Comparison with the turbulence profiles in 16 indicates that this is a laminar separation and that the turbulence appears downstream of the laminar separation position. This separated region is the reason that the lower surface has a thicker boundary layer. The low turbulence results are in agreement with the observations of Franc and Michel indicating that this prediction is qualitatively in agreement with the experiment while the results at the higher turbulence level (which is more representative of 'typical' conditions) are not.

The pressure distributions on the hydrofoil for these two cases are shown on Fig. 18. The change in the turbulence level causes some changes in the pressure distribution near the aft end of the hydrofoil where the flow separates from the surface.

Finally, a comparison with the results of Franc and Michel is given on Fig. 19. In this figure, the locations of several boundary layer events are tracked as a function of the angle of attack between negative ten and positive ten degrees. In particular, the plot shows the location of the laminar separation point, the start of transition to turbulence, the end of transition and the location of turbulent separation on the upper side of the airfoil. As an example, the laminar separation point on the upper surface lies at about 90% chord when the angle of attack is minus ten degrees. As the angle of attack is increased, the laminar separation point moves forward in an approximately linear fashion until the zero-degree angle is reached. At zero degrees, the location of laminar separation is at about 80% chord. As the angle of attack becomes positive, the point of laminar separation continues to move forward, but is very rapidly overtaken by the start of transition to turbulence at which point laminar separation ceases to exist.

Representative predictions from the present computations are included on Fig. 19 at -3, 0, and +3 degrees angle of attack. The location of the laminar separation point is seen to track the France and Michel results quite well at the -3 and the 0 degree locations. At the +3 angle of attack, laminar separation is not observed on the upper surface, again in agreement with the experimental results.

Results for the 'start' of transition are also indicated for the three angles of attack. The computational results for the start of transition are seen to track the Franc/Michel results qualitatively, although they are some 5% downstream of the Franc/Michel results. This

difference in location probably arises because of different methods for identifying the start of transition. The k-e model does not provide a direct measure of 'transition' and it must be inferred from the velocity profiles. The computed results do show that the transition location moves forward gradually in the negative angle of attack region, and then moves much more rapidly in the positive angle of attack region.

Finally, the computations show a single turbulent separation point at the positive angle of attack location. This turbulent separation point occurs at about 95% chord. Again, the absence of turbulent separation (on the upper side) at the -3 and 0 degree angle of attack cases is in agreement with the experimental observations. Overall, the present results indicate that the turbulence model can reproduce the observed turbulence conditions on the hydrofoil in the fully wetted condition and provide an appropriate background for employing a cavitation model.

A substantial amount of cavitation results from the single-phase and the two-phase models has been presented in Ref. 3 and shows that the two models give reasonable predictions of cavitation for various conditions. The two-phase model provides capability for the quasi-equilibrium results observed in numerous experiments and so is the preferred model for additional calculations.
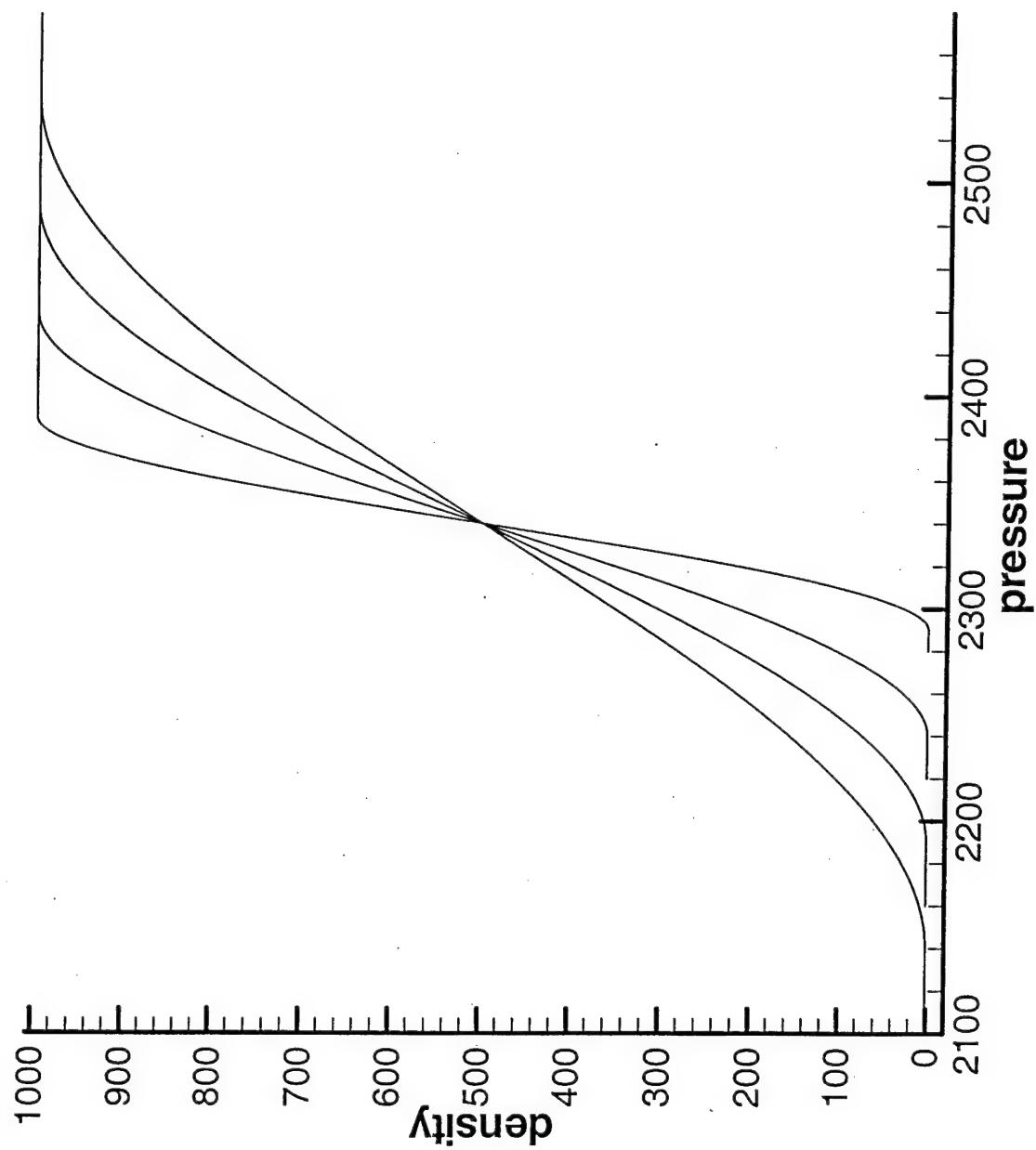
Fig. 1. Density-pressure curves in transition region for continuous equation of state used in the single-fluid model. $\Delta p = 100, 200, 300$ and $400 \ N/m^2$.

22
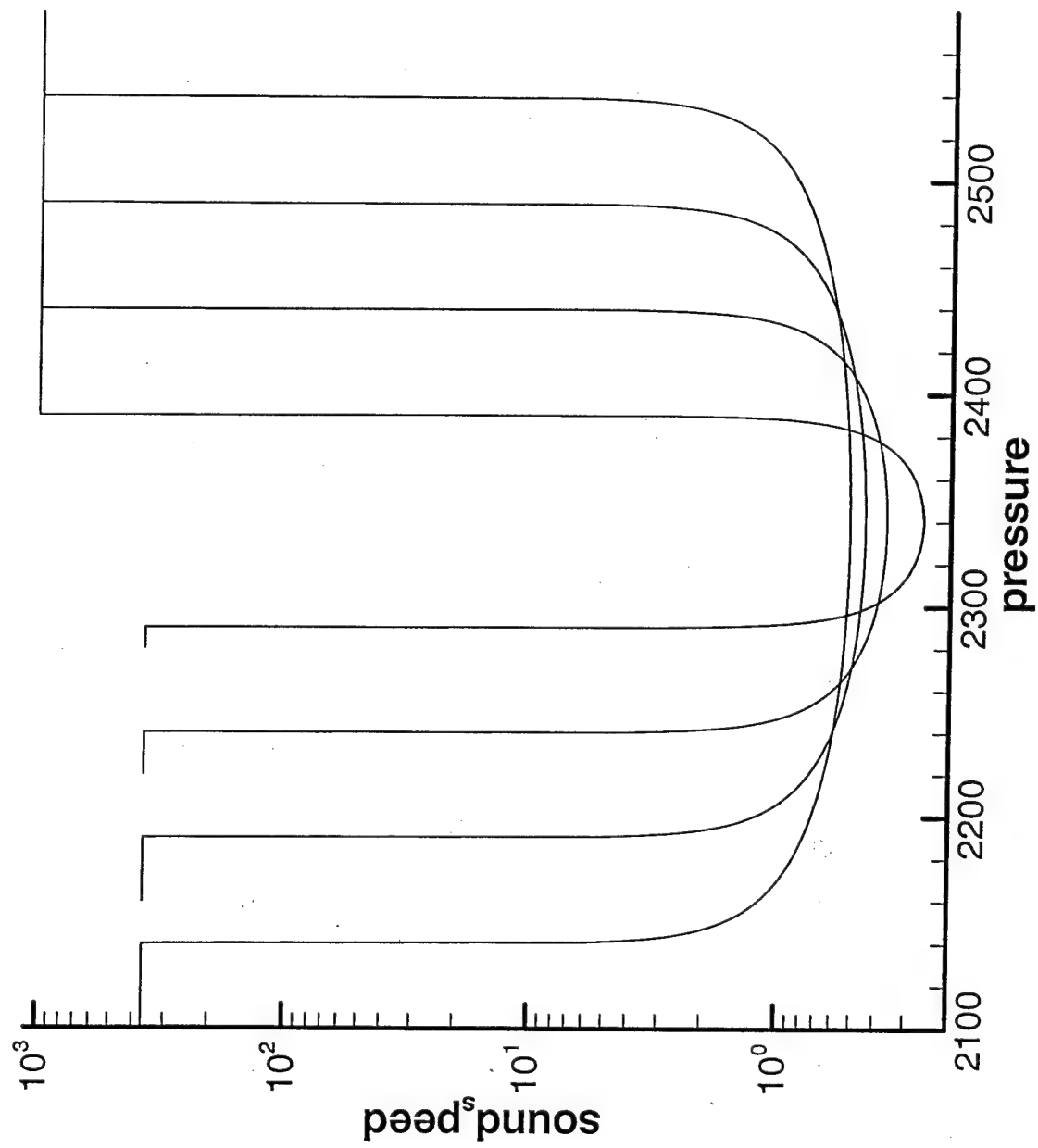
Fig. 2. Logarithm of the speed of sound of continuous equation of state as a function of pressure in transition regime. $\Delta p = 100, 200, 300$ and $400 \ N/m^2$.

23
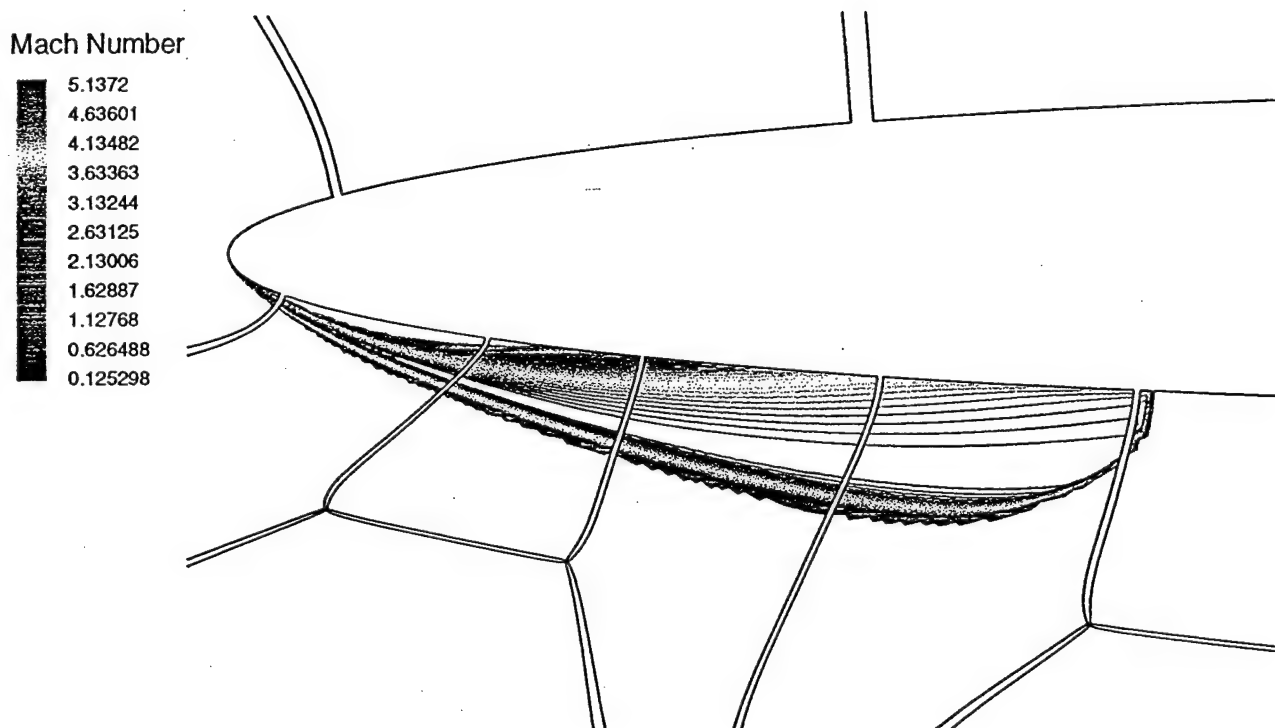
Fig. 3. Mach number contours for flow over an ellipse at −2
degrees angle of attack based on single-phase cavitation
model. Transonic flow region outlines cavitation zone.

$$K = \frac{K_v}{K_l} = \frac{1}{(\alpha + \rho_v / \rho_l)}$$
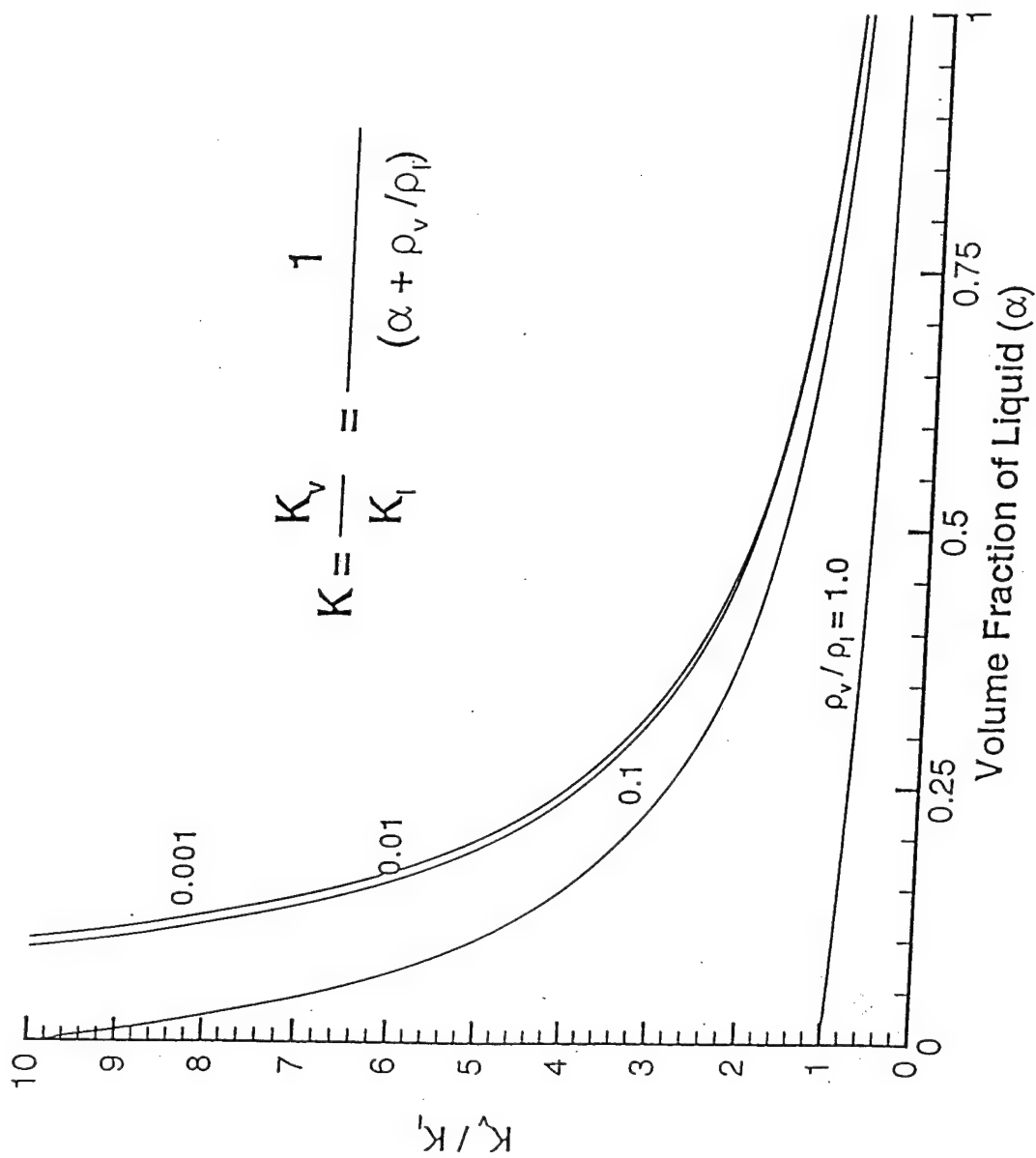
Fig. 4.   Ratio of K_v / K_l for various vapor to liquid density ratios as a function of volume fraction of liquid.

25
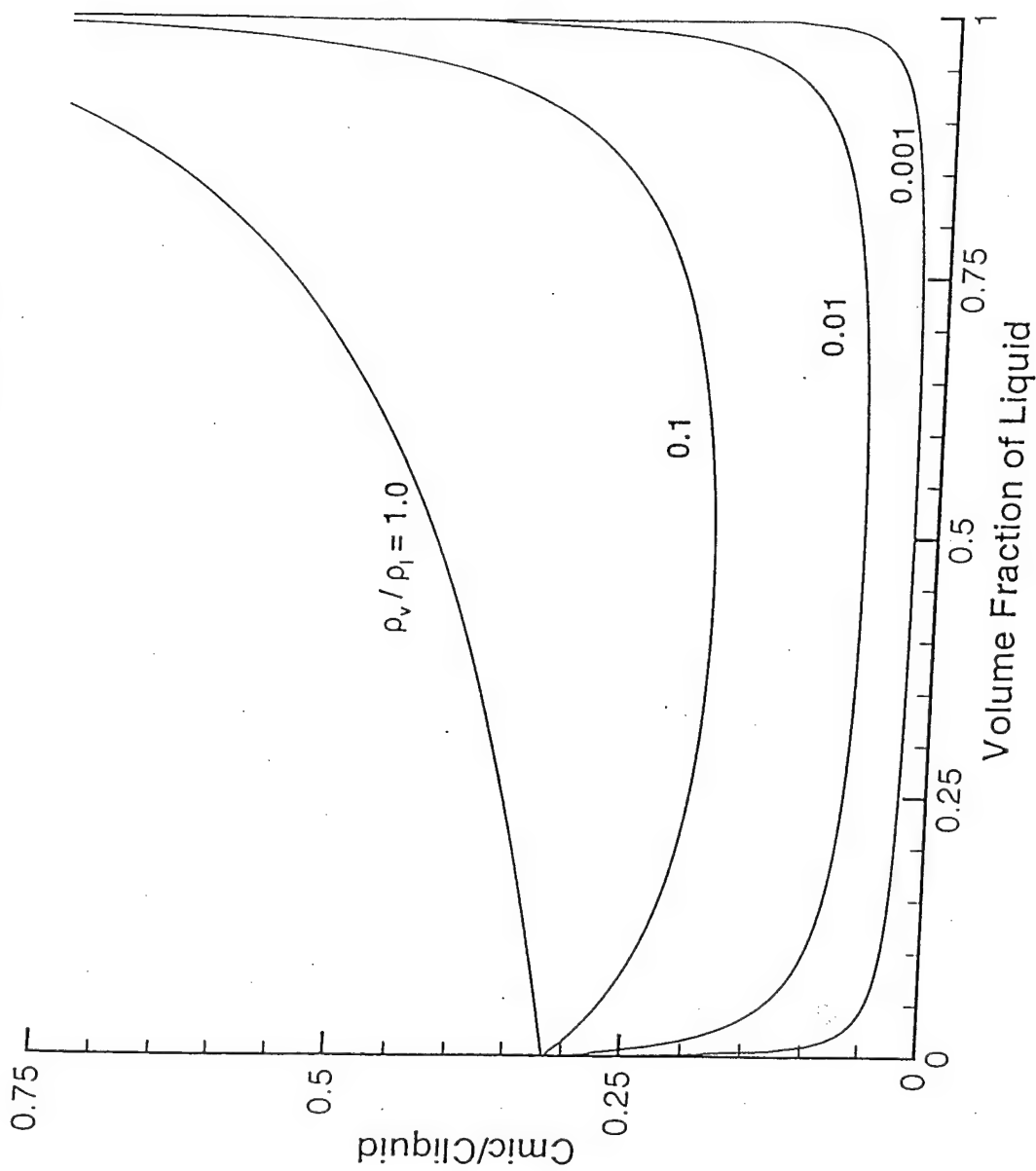
Fig. 5. Ratio of speed of sound in two-phase mixture to sound speed in liquid as a function of volume fraction of liquid for various ratios of vapor-to-liquid density ratios.

26

NACA 16-012 Hydrofoil

- 30 Blocks

- Various angles-of-attack

- 30,000 Grid Points
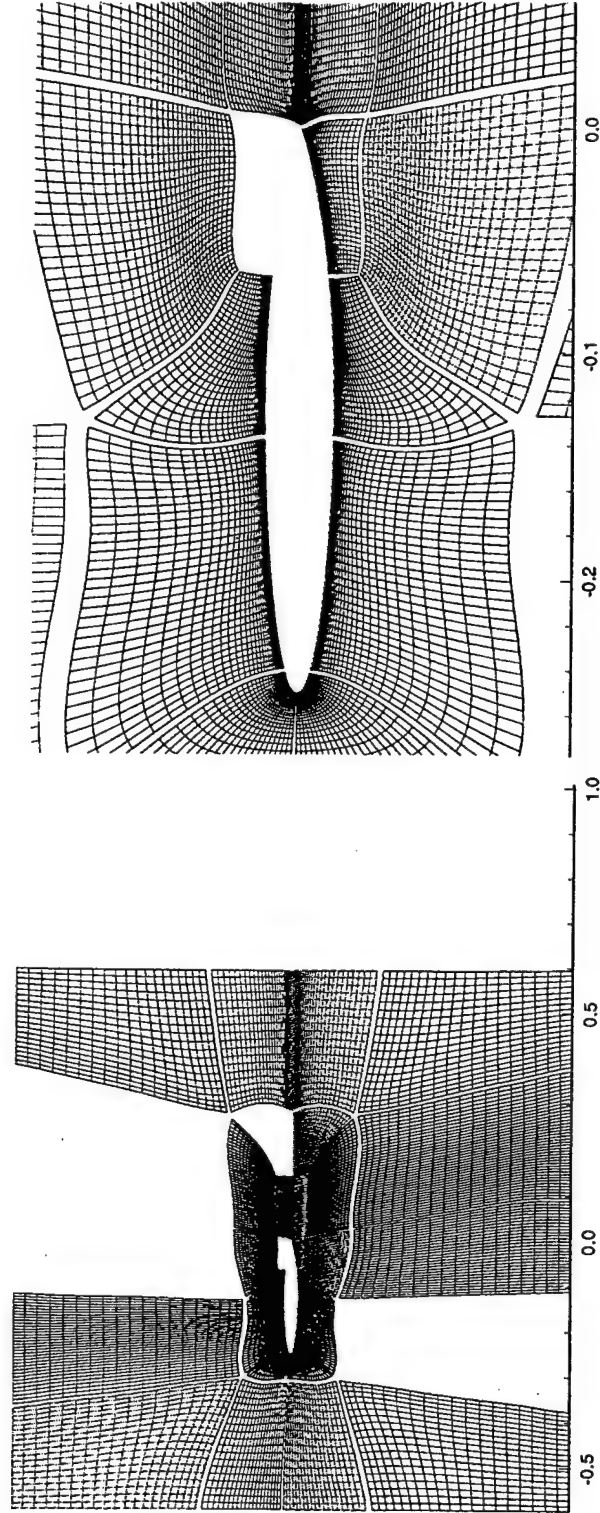
Fig. 6. Far-field and near-field views of multi-block grid for NACA 16-012 hydrofoil. 30 blocks, 30,000 grid points.

27

NACA 16-012 Hydrofoil

o 30 Blocks
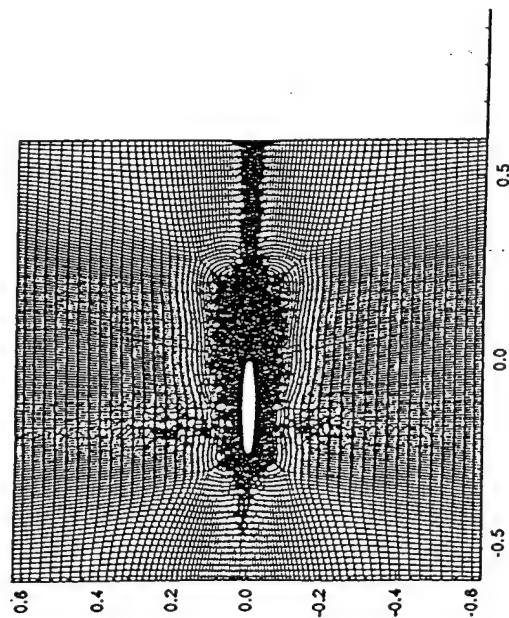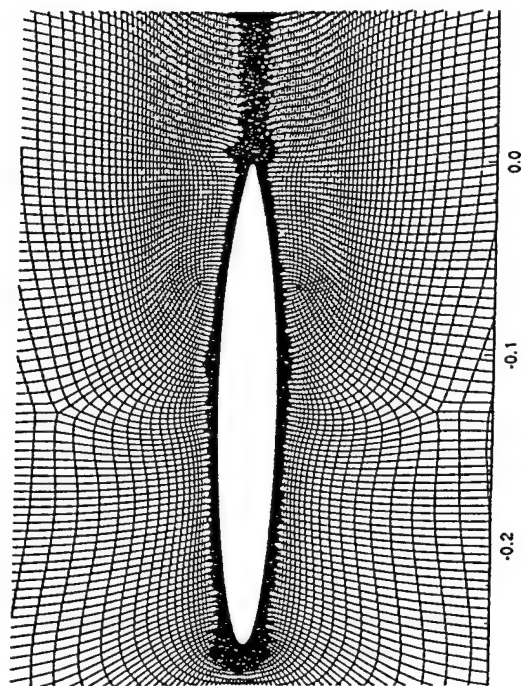
o 30,000 Grid Points

Fig. 7. Far-field and near-field views of single-block grid for NACA 16-012 hydrofoil. 30,000 grid points.

28

NACA 66(MOD) AIRFOIL

- 4 Degree angle-of-attack
- Cavitation number = 0.91
- Reynolds Number = 1.0x10^6

- Dual-Species Model
- Density Ratio = 100

Density

0.9
0.8
0.7
0.6
0.5
0.4
0.3
0.2
0.1
0

Pressure

75
60
45
30
15
0
-15
-30
-45
-60
-75
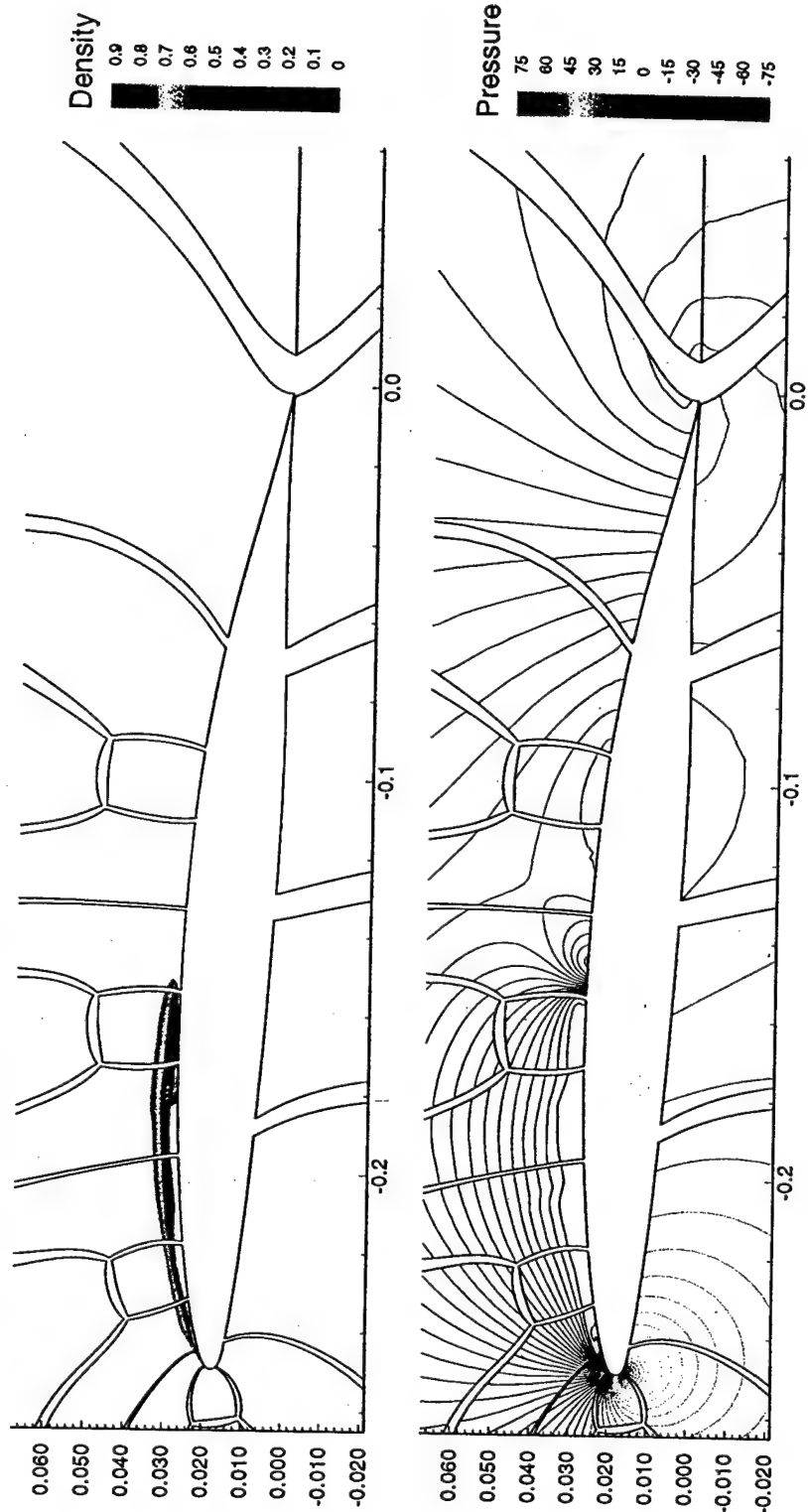
Fig. 8.   Computed density and pressure contours on a NACA 66 hydrofoil based upon the two-phase model. $\alpha = 4$ degrees; $\sigma = 0.91$;   Re = 1x106; $\rho_L / \rho_g = 100$.

CLOSE-UP OF RECIRCULATION

- 4 Degree angle-of-attack
- Cavitation number = 0.91
- Reynolds Number = 1.0x10^6
- Dual-Species Model
- Density Ratio = 100
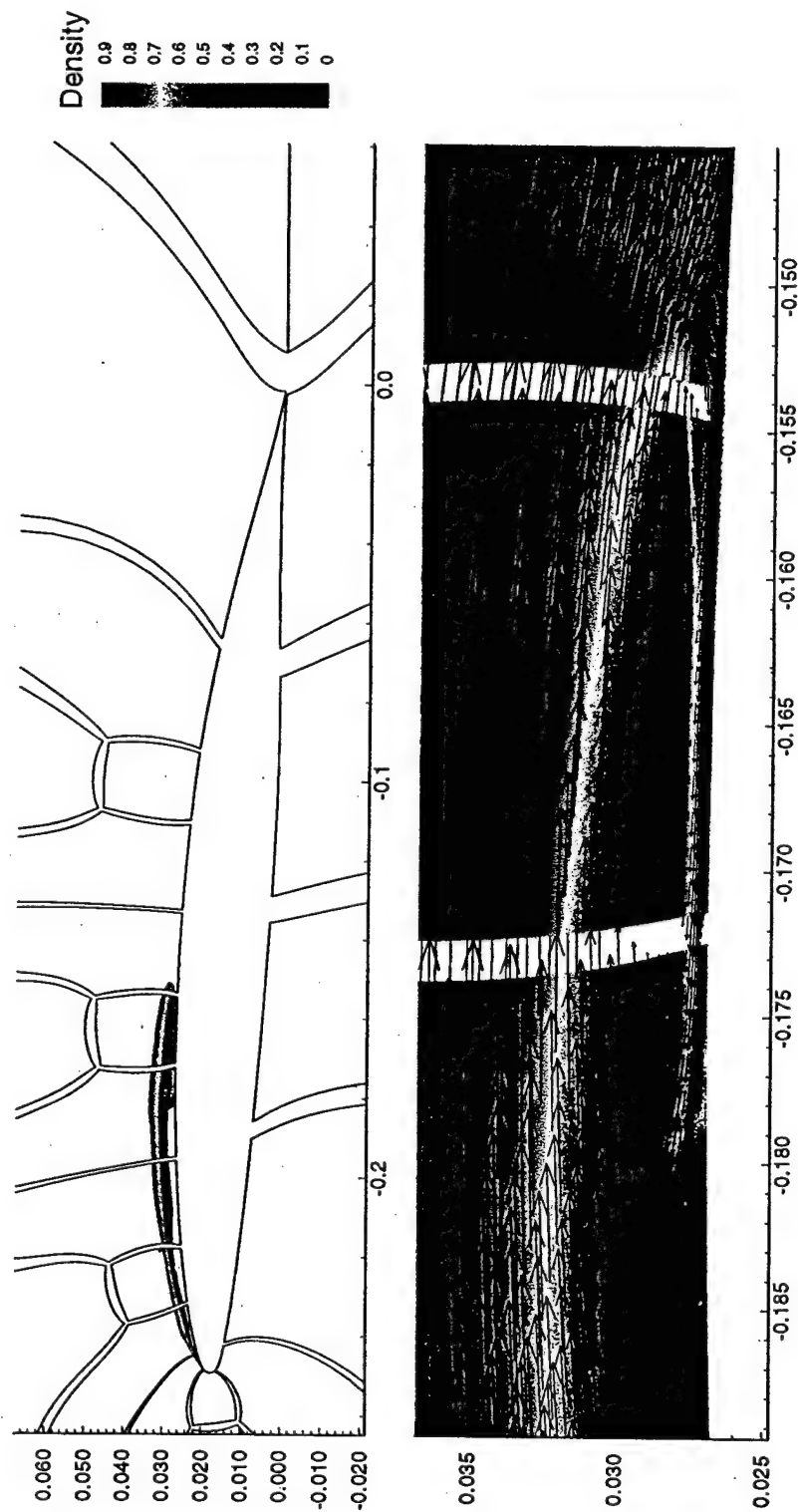
Fig 9.   Near-field view of cavitation region in Fig. 5 including velocity vectors and density contours.

30

WALL PRESSURE FOR WEDGE CASE

- 26.6 degree wedge

- Non-cavitating and Cavitating wall pressures

- Plotted from top of wedge to the downstream boundary
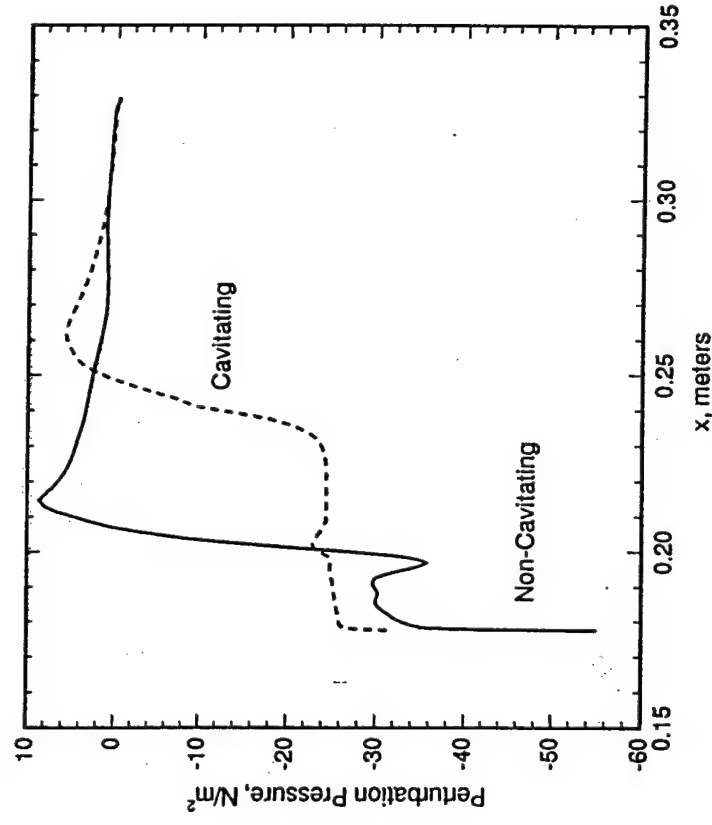
Fig. 10. Computed cavitating and non-cavitating wall pressure distribution on a 26.6 degree wedge.

31
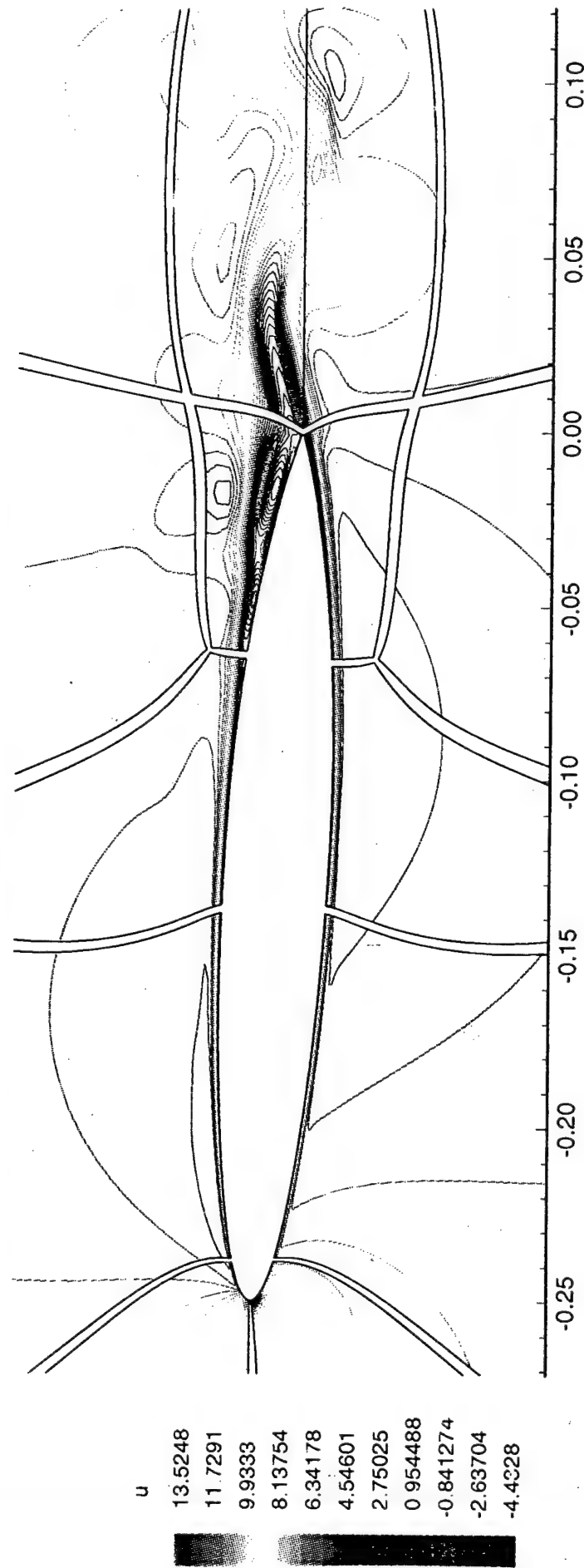
Fig. 11. Instantaneous snapshot of stream-wise velocity contours for laminar flow past a NACA 16-012 hydrofoil at a chord Reynolds number of 75,000.

NACA 16-012 Hydrofoil

- 0 Degree angle-of-attack
- 3rd-order differencing

- Re = 300,000
- 2-eq Turbulence model

U-velocity, m/s

Ratio of Turb. to Lam. viscosity

u
13.097
11.5338
9.97064
8.40746
6.84428
5.2811
3.71791
2.15473
0.591552
-0.971629
-2.53481

nut
211.065
190.639
170.214
149.788
129.362
108.937
88.5111
68.0855
47.6598
27.2342
6.80853
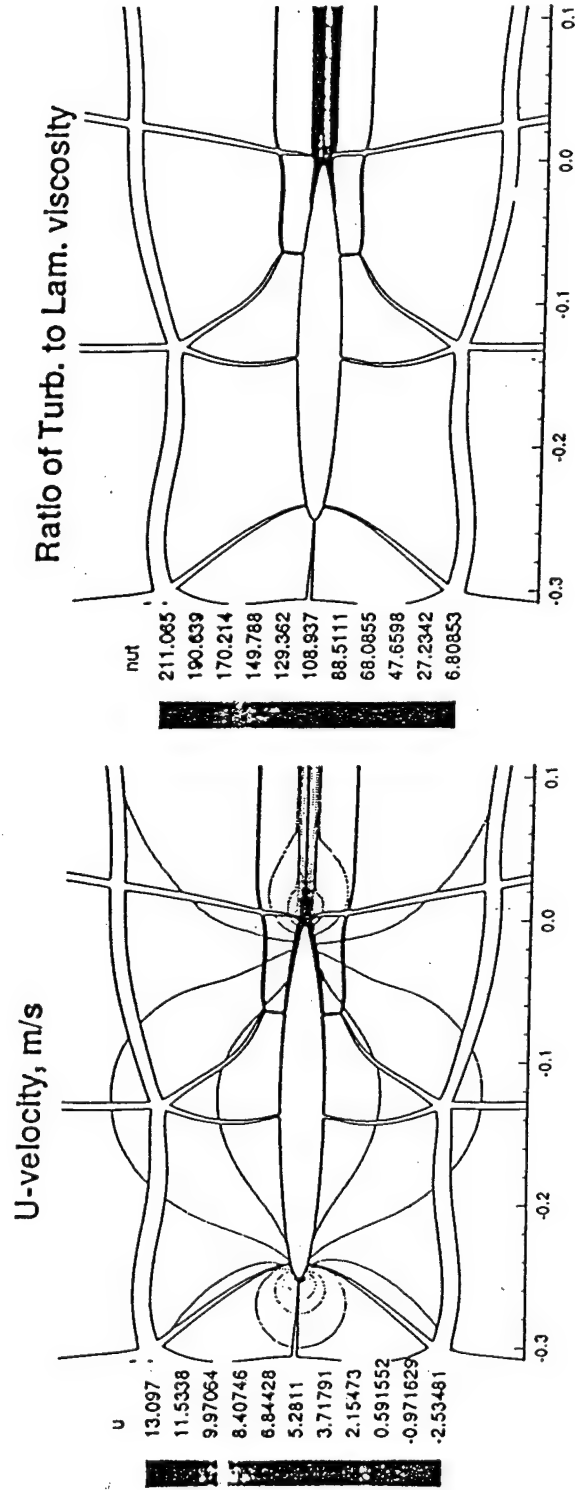
Fig. 12. Velocity contours and the ratio of eddy viscosity to laminar viscosity for the NACA 16-012 hydrofoil. Zero degrees angle of attack; Re = 300,000.

33

NACA 16-012 Hydrofoil

- 3 Degree angle-of-attack

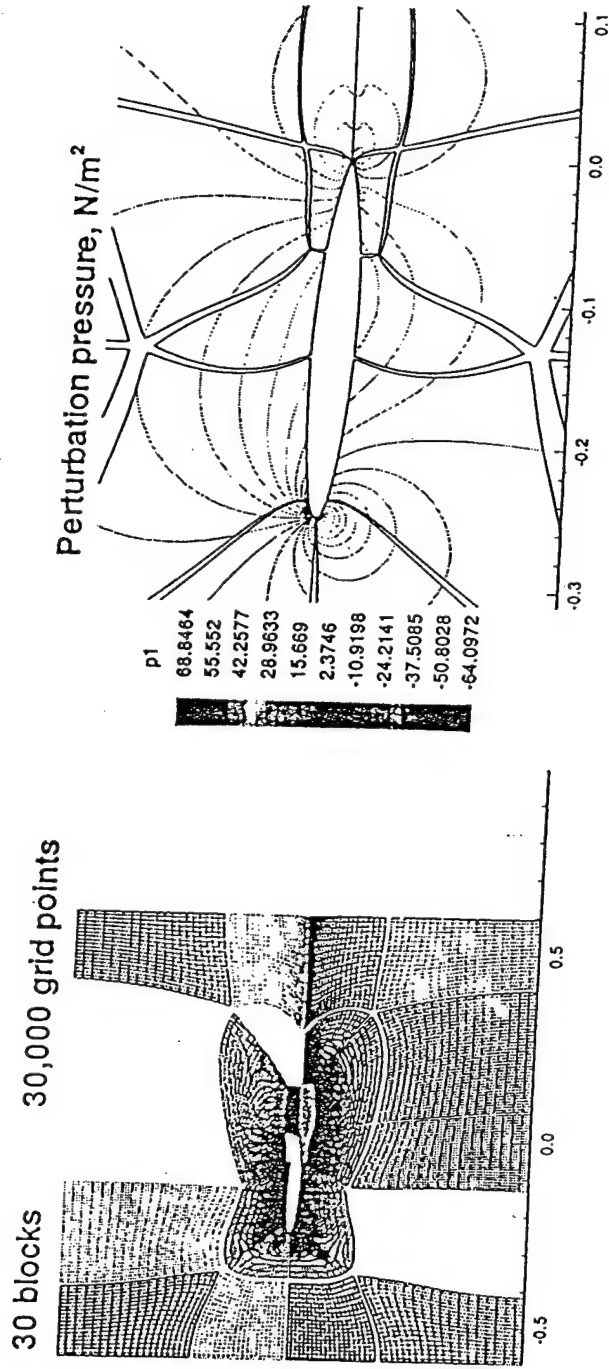- Re = 300,000

- 3rd-order differencing

- 2-eq Turbulence model

U-velocity, m/s

Ratio of Turb. to Lam. viscosity

u
15.1501
13.4422
11.7342
10.0263
8.31833
6.61039
4.90245
3.19451
1.48656
-0.221378
-1.92932

nut
172.175
155.513
138.851
122.189
105.527
88.8645
72.2024
55.5403
38.8782
22.2161
5.55403
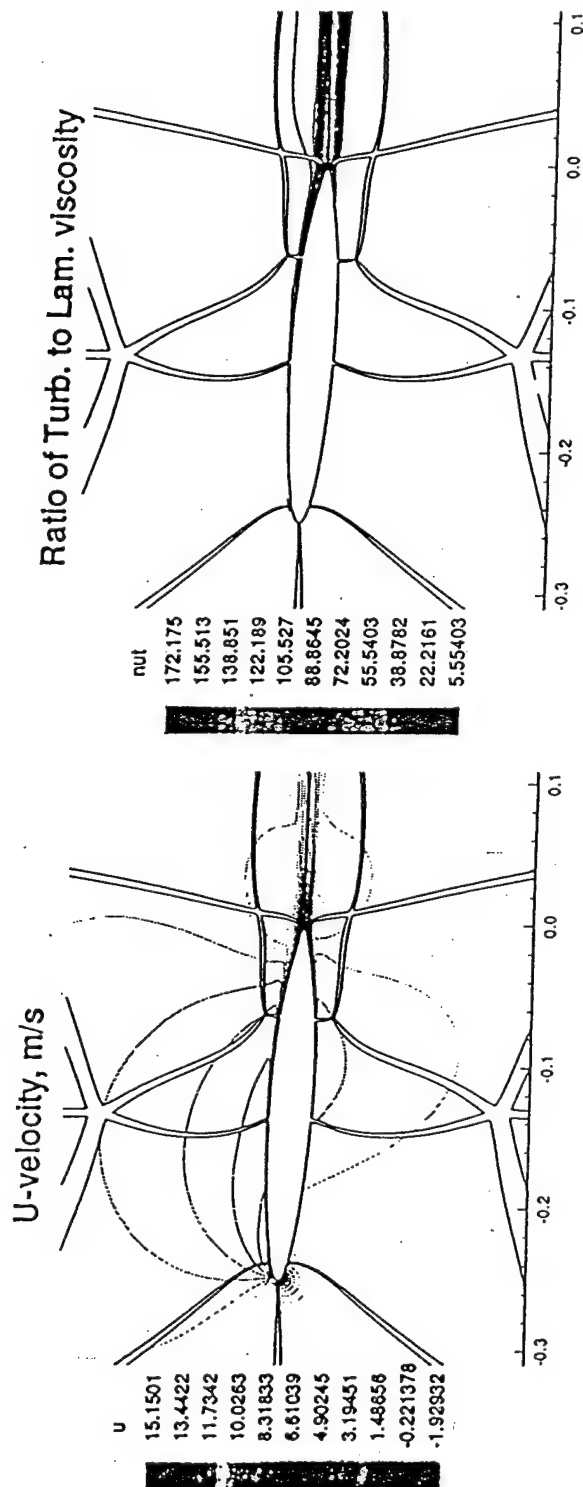
Fig. 13. Velocity contours and the ratio of eddy viscosity to laminar viscosity for the NACA 16-012 hydrofoil. Three degrees angle of attack; Re = 300,000.

34

NACA 16-012 Hydrofoil

- 3 Degree angle-of-attack

- Re = 300,000

- 3rd-order differencing

- 2-eq Turbulence model

Fig. 14. Multi-block grid and pressure contours for turbulent flow past a NACA 16-012 hydrofoil at three degrees angle of attack; chord Reynolds number, 300,000.
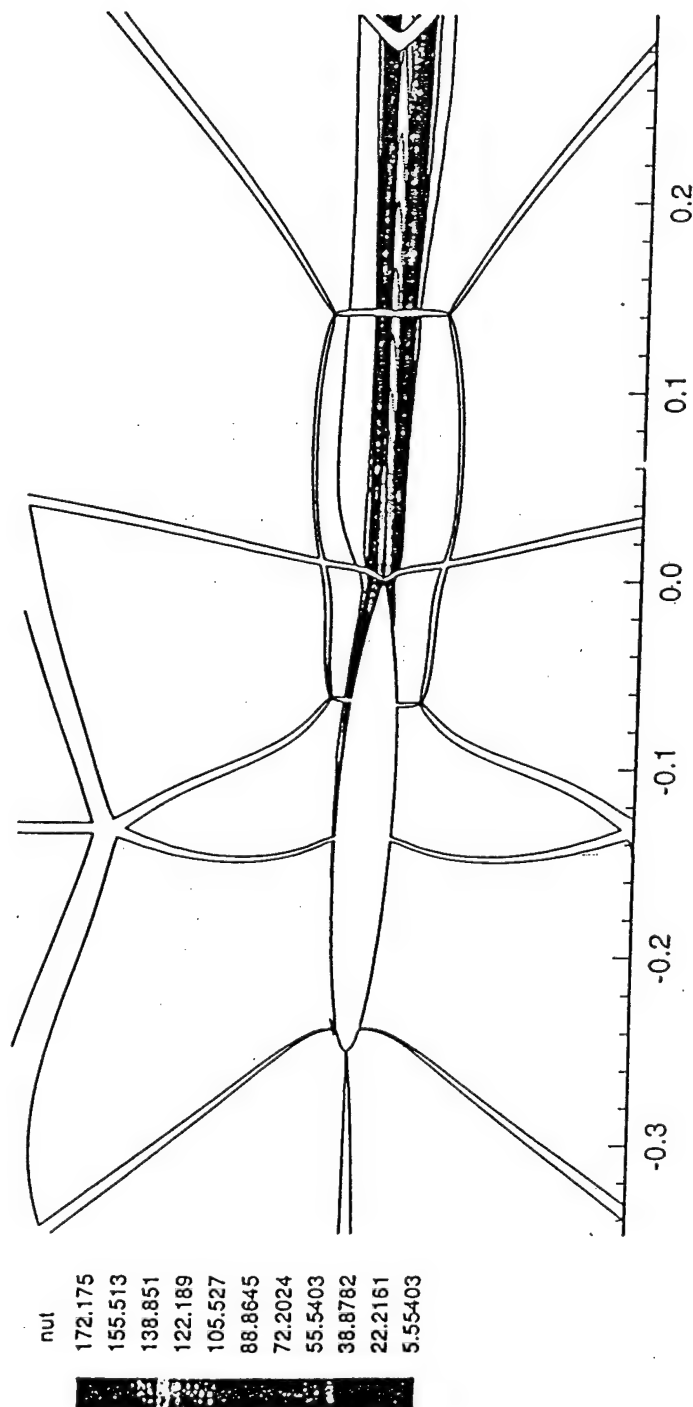
35

Fig. 15. Detailed view of the turbulent viscosity contours at three degrees angle of attack, Re = 300,000.

36

Trailing Edge Separation

- Re = 300,000
- 2-eq Turbulence Model

- Low freestream turbulence

0 Degree Angle-of-Attack

3 Degree Angle-of-Attack
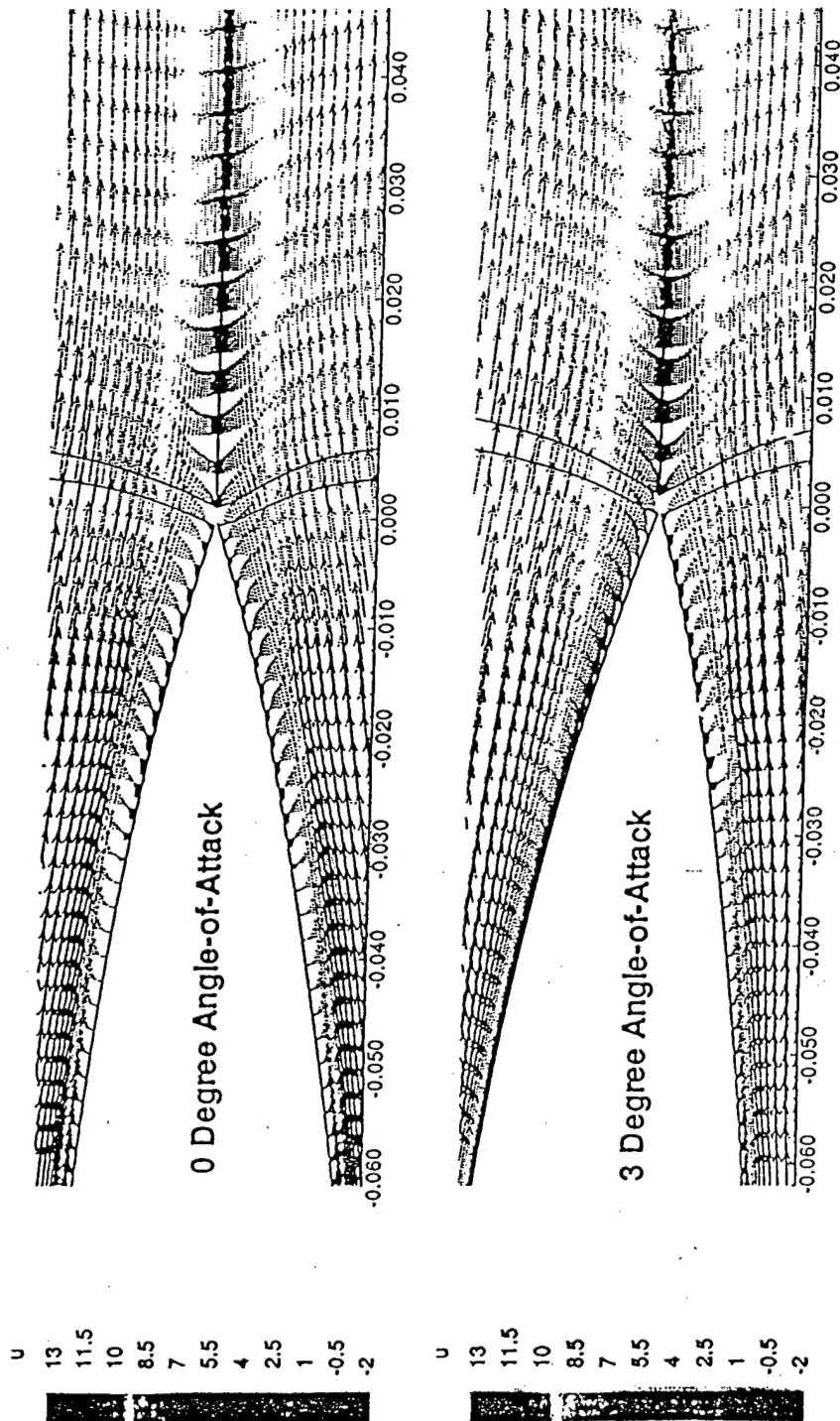
Fig. 16. Comparison of trailing edge region of NACA 16-012 hydrofoil zero and three degrees angel of attack. Low free-stream turbulence case.

37

Trailing Edge Separation

- Re = 300,000
- 2-eq Turbulence Model
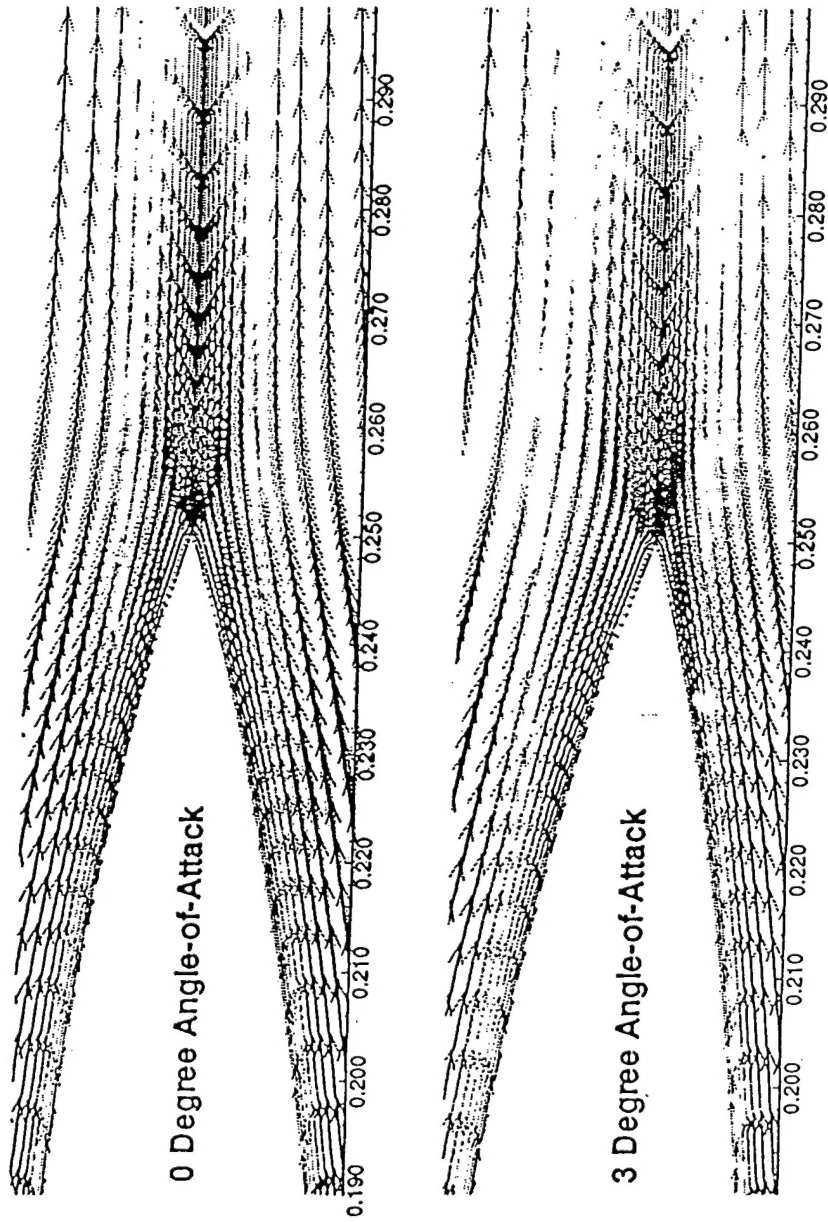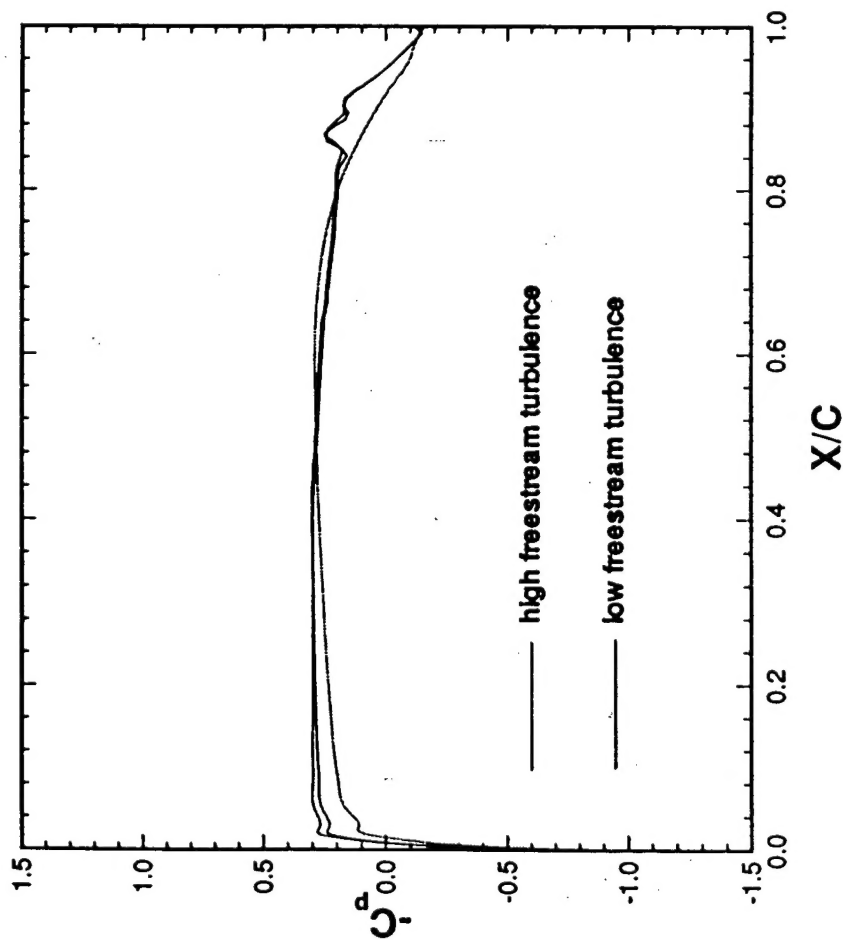- High freestream turbulence
- Explicit Algorithm

0 Degree Angle-of-Attack

3 Degree Angle-of-Attack

Fig. 17. Comparison of trailing edge region of NACA 16-012 hydrofoil zero and three degrees angel of attack. High free-stream turbulence case.

38

Pressure Coefficients for NACA 16-012

- Re = 300,000
- 2-eq Turbulence Model

0 Degree case
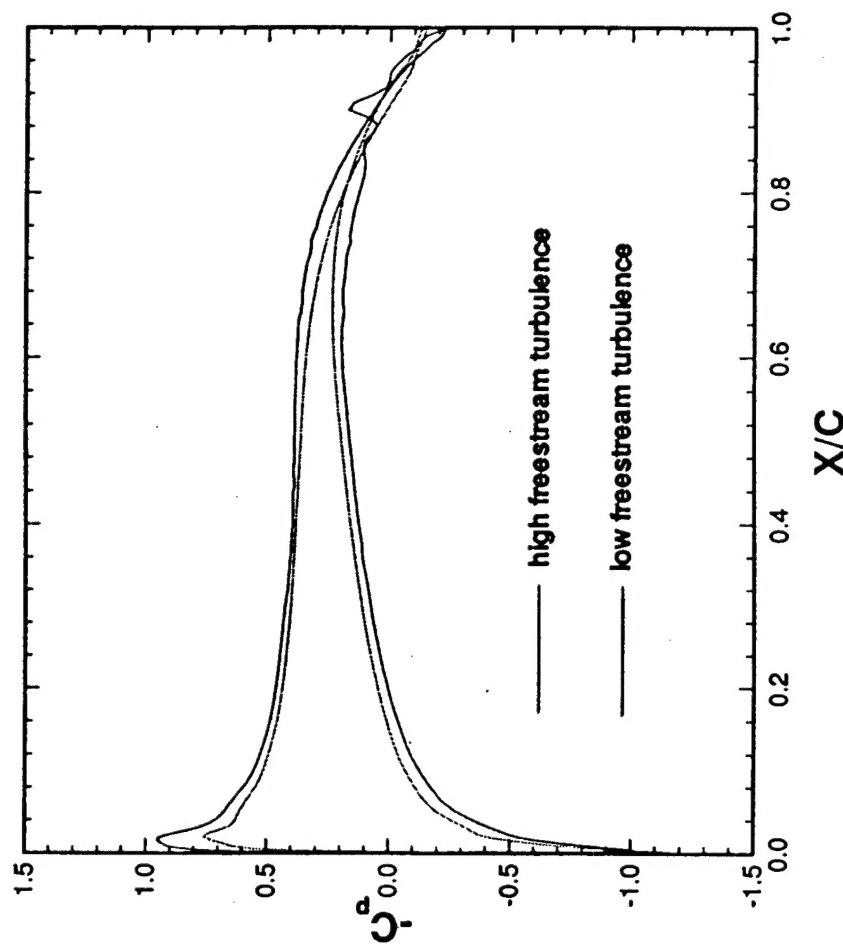
3 Degree case

Fig. 18.   Single block grid used for computation of high turbulence level solution.
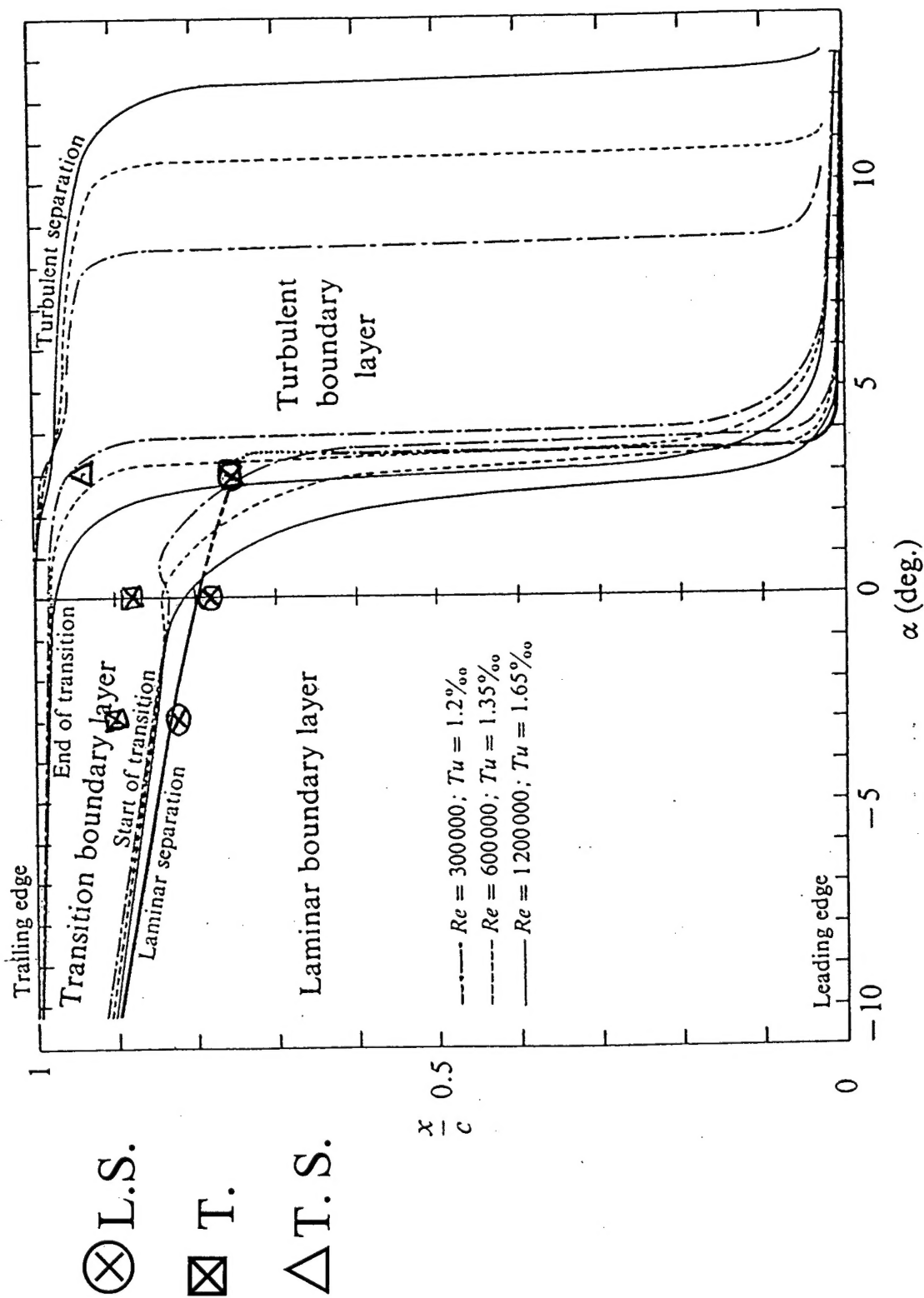
39

Attached cavitation and the boundary layer

Fig. 19. Position of boundary layer characteristics versus angle of attack. NACA 16-012 hydrofoil; Upper side.

40